

AD-A123 321

ANALYTICAL PREDICTION OF TURBULENT HEAT TRANSFER
PARAMETERS(U) COLORADO UNIV AT BOULDER DEPT OF
MECHANICAL ENGINEERING A BEJAN DEC 82 CUMER-82-6

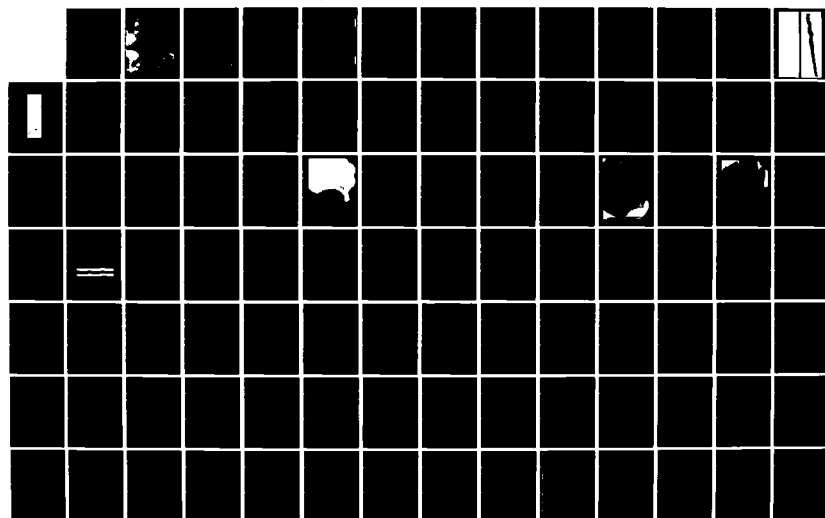
1/2

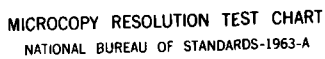
UNCLASSIFIED

N00014-79-C-0006

F/G 20/4

NL





MICROCOPY RESOLUTION TEST CHART
NATIONAL BUREAU OF STANDARDS-1963-A

AD A123321



**UNIVERSITY
OF
COLORADO**

Analytical Prediction of Turbulent
Heat Transfer Parameters:

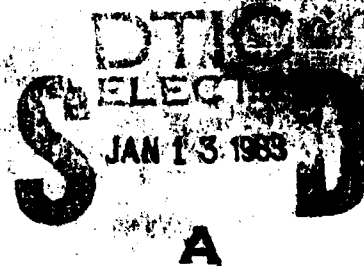
The Second Annual Report

Adrian Bejan

CUMER-82-6

December 1982

**DEPARTMENT OF
MECHANICAL ENGINEERING**



**College of Engineering
Boulder, Colorado**

This document has been approved
for public release and sale; its
distribution is unlimited.

83 01 13 019

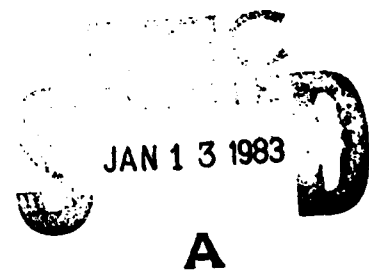
Analytical Prediction of Turbulent
Heat Transfer Parameters:

The Second Annual Report

Adrian Bejan

CUMER-82-6

December 1982



A

ANALYTICAL PREDICTION OF TURBULENT HEAT TRANSFER PARAMETERS:

THE SECOND ANNUAL REPORT

December 1982

Adrian Bejan
Associate Professor
Department of Mechanical Engineering
University of Colorado
Boulder, Colorado 80309

Prepared for

M.K. Ellingsworth
Program Monitor
The Office of Naval Research
Arlington, Virginia 22217

Under Contract No. N00014-79-0006, Work Unit 097-431. Approved for public release; distribution unlimited. Reproduction in whole or in part is permitted for any purpose of the United State Government.

REPORT DOCUMENTATION PAGE		READ INSTRUCTIONS BEFORE COMPLETING FORM
1. REPORT NUMBER CUMER-82-6	2. GOVT ACCESSION NO. AD-A125321	3. REPORT'S CATALOG NUMBER
4. TITLE (and Subtitle) Analytical Prediction of Turbulent Heat Transfer Parameters: The Second Annual Report		5. TYPE OF REPORT & PERIOD COVERED Annual - 10/1/81-9/30/82
7. AUTHOR(s) Adrian Bejan		6. PERFORMING ORG. REPORT NUMBER
9. PERFORMING ORGANIZATION NAME AND ADDRESS Department of Mechanical Engineering, Campus Box 427, University of Colorado, Boulder, CO 80309		8. CONTRACT OR GRANT NUMBER(s) N00014-79-C-0006
11. CONTROLLING OFFICE NAME AND ADDRESS Office of Naval Research 800 N. Quincy Street Arlington, VA 22217		10. PROGRAM ELEMENT, PROJECT, TASK AREA & WORK UNIT NUMBERS Program Element 61153N24 Project RR024-03, Task Area RR024-03-02, Work Unit NR097-431
14. MONITORING AGENCY NAME & ADDRESS (if different from Controlling Office)		12. REPORT DATE December 1982
		13. NUMBER OF PAGES 100
		15. SECURITY CLASS. (of this report) Unclassified
		15a. DECLASSIFICATION/DOWNGRADING SCHEDULE
16. DISTRIBUTION STATEMENT (of this Report) Approved for public release; distribution unlimited		
17. DISTRIBUTION STATEMENT (of the abstract entered in Block 20, if different from Report) Same as block #16		
18. SUPPLEMENTARY NOTES		
19. KEY WORDS (Continue on reverse side if necessary and identify by block number) Heat transfer, turbulent flow, irreversibility, buckling theory.		
20. ABSTRACT (Continue on reverse side if necessary and identify by block number) → The objective of this research is to construct a purely theoretical foundation for the phenomenon of turbulent heat transfer. In the present report the elastic buckling properties of inviscid flow are used to reconstruct classical features of turbulent behavior. The report contains also two experiments designed to visualize the buckling of high Reynolds number flow.		

SECTION 1 Theory of turbulent flow: the second year

During the past two years, my associates and I have focused on the newly discovered "elastic buckling" property of inviscid flow, as a way of providing the necessary building block in our quest to reconstruct theoretically the main features of turbulent fluid behavior. As summarized in the First Annual Report [1], the buckling property of inviscid flow is the concise result of accounting for the static equilibrium of a finite-size portion of an inviscid flow field. Any inviscid flow "fiber", like a jet, a wake or a shear layer, possesses a previously unknown length scale - the buckling wavelength - which is a certain multiple of the transversal dimension of the fiber. Buckling is a global property of the flow. As such, the buckling property accounts for the extremely common "meander" phenomenon and, as shown in the present report, for the "large scale structure" of turbulent flow. The new length and time scales revealed by the buckling property, the buckling wavelength and the buckling time or time of eddy formation, allows the turbulence thinker to reconstruct not only the geometry of turbulent flow but also the history.

The second year progress summarized in the present report stems from research conducted on two distinct fronts. The first front was touched on already during the first year, and represents the systematic application of the length and time scales of buckling to the task of predicting theoretically some of the best known features of turbulent behavior. In section 5 of the present report, the buckling property is used to account for century-old observations concerning the meandering of rivers and other streams. In section 6, the same theoretical framework serves as basis for explaining the large scale intermittent structure of turbulent shear flow, with special emphasis on

[1] A. Bejan, Analytical Prediction of Turbulent Heat Transfer Parameters, The First Annual Report, CUMER 81-3, Mechanical Engineering Department, University of Colorado, Boulder, December 1981.

the friction and heat transfer characteristics of turbulent boundary layer flow.

The second research front considered during the second year consists of experiments designed to visualize the buckling property of inviscid flow. Sections 3 and 4 of the present report outline two experiments that reveal the buckling property with amazing clarity. The basic rule in the design of the buckling visualization experiments is the prevention of the post-buckling evolution of the buckled inviscid stream, in other words, the prevention of the eddy-formation phase of the buckling process. More visualization experiments are currently underway and will be reviewed in the Final Report next year.

SECTION 2 List of second-year peer-refereed publications

1. A. Bejan, The Meandering Fall of Paper Ribbons, Physics of Fluids, Vol. 25, May 1982, pp. 741,742.
2. M.G. Stockman and A. Bejan, The Nonaxisymmetric (Buckling) Flow Regime of Fast Capillary Jets, Physics of Fluids, Vol. 25, September 1982, pp. 1506-1511.
3. A. Bejan, Theoretical Explanation for the Incipient Formation of Meanders in Straight Rivers, Geophysical Research Letters, Vol. 9, August 1982, pp. 831-834.
4. A. Bejan, Entropy Generation ^{through} Heat and Fluid Flow, John Wiley & Sons, New York, 1982.
5. A. Bejan, Second Law Analysis in Heat Transfer and Thermal Design, Advances in Heat Transfer, Vol. 15, 1982.
6. D. Poulikakos and A. Bejan, Fin Geometry for Minimum Entropy Generation in Forced Convection, Journal of Heat Transfer, Vol. 104, November 1982,
7. A. Bejan, Theory of Instantaneous Sinuous Structure in Turbulent Buoyant Plumes, Warme-und Stoffubertragung, Vol. 16, 1982, pp. 237-242.

SECTION 3

The Meandering Fall of Paper Ribbons *

by

Adrian Bejan
Department of Mechanical Engineering
University of Colorado
Boulder, Colorado 80309

Abstract

This note discusses experimental observations of the meandering fall of light-weight tissue paper ribbons. The photographs show that the ribbons assume a sinusoidal shape with a unique wavelength which scales with the thickness of the airstream entrained by the ribbon.

*published in Physics of Fluids, Vol.25(5), May 1982, pp.741,742.

The objective of this note is to present a series of interesting experimental observations concerning the meandering motion executed by highly flexible ribbons falling through the air. The experiment consisted of dropping a length of light-weight toilet tissue paper through the air and photographing its shape as it falls to the ground. The reader may take note of the fact that this falling-ribbon phenomenon occurs naturally when excited sports fans launch rolls of tissue paper from the stands onto the playing field. Another natural phenomenon related to the falling-ribbon experiments described in this note is the "waving of flags"¹ and the "vibration" of tape drives used in the computer technology.² The classical perspective in the study of flag waving falls in the realm of Hydrodynamic Stability Theory, where one questions the stability of the flexible solid surface. The starting point in the stability study is the assumption of an initial deformation of arbitrary wavelength.

In the present experiments, ribbons of various lengths were dropped from heights in the range 3-7m, through the quiescent air of the laboratory. The time of free fall was measured with a digital stopwatch; it was found that the ribbon reached its terminal velocity very quickly, therefore, the free-fall velocity U could be determined by dividing the total travel by the measured time of free-fall. In order to force the ribbon to fall "head first", one end was loaded with a lead refill for a mechanical pencil.

This simple experiment was repeated many times and, in all cases, the photographs showed that the falling ribbon acquires a sinuous shape: the wavelength of this shape was the same for all the cases involving a ribbon of fixed length. Figures 1(a) and 1(b) show very clearly the characteristic sinuous shape observed in these experiments. A longer ribbon (Fig. 1b) exhibits a relatively longer wavelength.

Another important observation is the fact that the sinuous shape travels as a solid body downward, at a speed of order $U/2$, where U is the speed of the tissue paper itself. The wave speed was measured photographically, as shown in Fig. 2. This photograph was obtained with the shutter open in complete darkness, while lighting the falling ribbon with a strobe light three times, at precise time intervals ($t = 0.025$ s). The fact that the sinuous shape travels at half speed is strong evidence that the sinuous shape is produced not by the tissue paper, but by the airstream whose centerline moves at top speed U through an ambient at rest.

The key measurement facilitated by the falling-ribbon experiment is that of the meander wavelength. Measuring the distance between the elbows of the sinuous shape of Figs. 1(a) and 1(b), and averaging these measurements over the sinuous portions of each ribbon, yields the wavelengths listed under λ_B in Table 1. The relatively small standard deviations of these measurements indicate that the elbow-to-elbow distance does not vary appreciably along the wavy portion of the ribbon.

The effective thickness D_e of the air stream entrained by the ribbon can be calculated based on the following energy-conservation argument. During its steady fall at terminal velocity U , the ribbon weight W performs the mechanical work $W\Delta L$ on its ambient; ΔL is the linear increment in downward travel, equal to $U\Delta t$, where Δt is the time increment. The work done by the weight is first converted into the kinetic energy imparted to the airpacket pierced by the tip of the ribbon during the time Δt (at the same time, the ribbon-air train sheds a moving air packet of the same size: the kinetic energy of this air packet is eventually dissipated in the wake). Equating the two energy increments, we write

$$W\Delta L = (\rho D_e \Delta L b) \frac{U^2}{2} \quad \text{or} \quad D_e = 2 \frac{W}{\rho U^2 b} \quad (1)$$

where b is the ribbon width and ρ is the air density. The results of this calculation are listed in Table 1. Clearly, the meander wavelength scales with the air stream thickness.

A possible explanation for the above observations may be offered based on the buckling theory of inviscid streams.^{3,4} One key result of this theory is the universal proportionality which must exist between stream thickness (D) and "buckling" wavelength (λ_B). For a two-dimensional stream one finds $D = (\sqrt{3}/\pi) \lambda_B$, which agrees in an order of magnitude sense with the measurements listed in Table 1. Additional evidence supporting this explanation is the fact that, from Fig. 1(a) to Fig. 1(b), both λ_B and D_e increase.

Acknowledgement. This research work was supported by the Office of Naval Research.

References

1. H. Lamb, Hydrodynamics, Dover, New York, 374 (1945).
2. S.K. Datta and W.G. Gottenberg, J. Appl. Mech., 97, 195 (1975).
3. A. Bejan, Letters in Heat and Mass Transfer, 8, 187 (1981).
4. A. Bejan, Phys. Fluids, 24, 1764 (1981).

Table I

Experiment	Ribbon dimensions length x width $L \times b$ [cm ²]	Total weight W [g]	Terminal speed $U[\frac{m}{s}]$	Meander wavelength λ_B [cm]	Effective air-stream thickness D_e [cm]
Fig. 1(a)	125 x 11.4	3.21	2.93 ± 0.15	15.5 ± 1.3	5.5 ± 0.56
Fig. 1(b)	183 x 11.4	4.97	3.04 ± 0.09	28 ± 1.5	7.86 ± 0.46

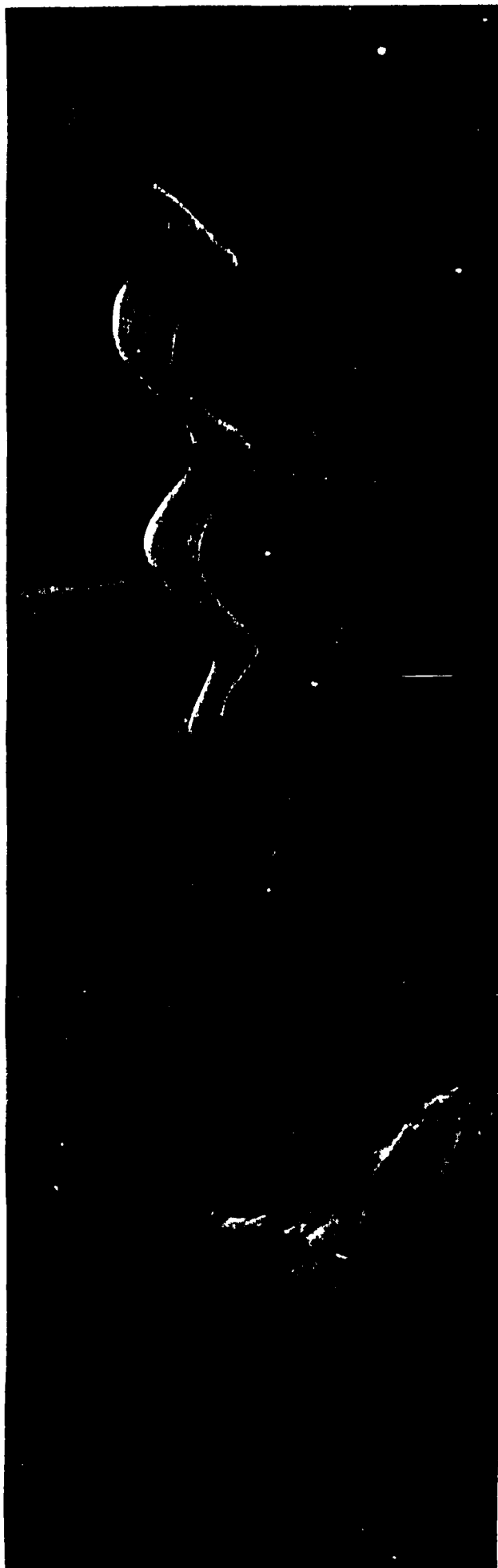


Fig. 1

SHAPE
TRAVEL

1 →
2 →
3 →



← 1

← 2

← 3

PAPER
TRAVEL

Fig. 2

SECTION 4

THE NONAXISYMMETRIC (BUCKLING) FLOW REGIME OF FAST CAPILLARY JETS *

by

Michael G. Stockman and Adrian Bejan

Department of Mechanical Engineering
University of Colorado
Boulder, Colorado 80309Abstract

This paper reports an experimental study of the nonaxisymmetric flow of a fast liquid jet discharging into the atmosphere. The nonaxisymmetric shape of the jet was photographed and subjected to a wavelength analysis. The results of the wavelength analysis demonstrate that the jet shape is governed by a narrow band of wavelengths associated with a characteristic value λ_{\max} which scales with the jet diameter D . It is shown that the experimental observations are in agreement with predictions based on hydrodynamic stability theory and buckling theory.

* published in Physics of Fluids, Vol.25(9), September 1982, pp.1509-1511.

I. Introduction

The problem of capillary jet flow and break-up has a long history beginning with the qualitative studies of Bidone¹ and Savart², which were extended by Savart, Plateau, and Rayleigh, and summarized later by Rayleigh³. These studies focused on the low speed regime where the jet forms radially symmetric, regularly shaped, drops of measurable frequency. Rayleigh studied the symmetric (varicose) break-up theoretically, by imposing hypothetical infinitesimal disturbances on the jet and examining the stability (or instability) of each disturbance in time. Rayleigh's theory was summarized and extended in several directions by Chandrasekhar⁴.

Much of the post-Rayleigh work focused almost exclusively on the axisymmetric (varicose) regime, although there have been a number of instances in which a nonaxisymmetric break-up mode was observed. Crane, Birch, and McCormick⁵ employed an electronically driven vibrator to study the dispersion curve of low speed jets (the dispersion curve is the graphical representation of the response of the capillary jet to a continuous set of imposed disturbance frequencies). Their results agreed only qualitatively with Rayleigh's. A similar experiment was described by Donnelly and Glaberson⁶, who studied the response of a capillary jet to external disturbances generated by a loudspeaker and audio oscillator. Donnelly and Glaberson, like Crane *et al.*, noted parcels of liquid between the large drops predicted by Rayleigh's theory. They termed these parcels as "ligaments" and accounted for their appearance by arguing that the ligaments were due to higher order harmonics present in the disturbing frequency. Donnelly and Glaberson found excellent agreement between Rayleigh's linearized theory and their experimental results, despite

the fact that Rayleigh's theory does not predict the existence of ligaments.

During the past fifteen years we have witnessed a large volume of research aimed at explaining and predicting the formation of ligaments in the process of varicose break-up; examples of this research effort are the theoretical work of Yuen ⁷ , Nayfeh ⁸ , and Lafrance ⁹ . Experimentally, the ligament and satellite drop formation mechanism was investigated by Goedde and Yuen ¹⁰

Rutland and Jameson ¹¹ and, in a comprehensive three-paper study, by Chaudhary and Redekopp ¹² and Chaudhary and Maxworthy ^{13,14} .

Relative to the wealth of information on the varicose regime, the non-axisymmetric break-up is practically unknown. Photographs of the meandering path of fast capillary jets appeared as early as 1931 in the writings of Weber ¹⁵

and Haenlein ¹⁶ : these photographs were reproduced later in a famous textbook by Prandtl ¹⁷ who referred to the crests of the nonaxisymmetric shape as "wavy bulges". The subject of nonaxisymmetric break-up resurfaced only recently in the literature, triggered by the need for improved fire fighting equipment. Hoyt, Taylor, and Runge ¹⁸ reported an experimental study of the break-up of fast water jets and on the effect of adding drag reducing polymer to the water solution. The authors refer to the meandering section of the jet as an "unstable wave region". Greater photographic resolution of the meandering break-up regime was achieved in a subsequent descriptive study by Hoyt and Taylor ¹⁹ .

In summary, much of the existing work on the break-up of capillary jets has dealt with the axisymmetric (varicose) regime. The work on the non-axisymmetric regime is sketchy and, in all cases, qualitative. The object of this paper is to report a quantitative study of the nonaxisymmetric flow regime of fast capillary jets. For the first time, the photographed shape of such jets is subjected to a rigorous wavelength analysis which shows conclusively that the nonaxisymmetric shape is governed by a characteristic, meander-type, wavelength which scales with the jet diameter.

II. Experiment

The break-up modes of a capillary jet issuing into the surrounding atmosphere were studied in the laboratory using the apparatus shown in Fig. 1. The fluid reservoir consisted of a 1.83 m tall Plexiglas cylinder with an internal diameter of 14 cm. The reservoir had a number of fluid drainage ports distributed equidistantly over its height. The nozzle adaptor included a "rounded" internal duct design, and was located 15 cm from the bottom of the cylinder in order to avoid the flow distortion caused by the bottom. The reservoir was safely pressurized to 2 atm (30 psig) while the cylinder was full, yielding a jet velocity range of 0-25 m/s. The range of low jet velocities was produced without pressurization, by controlling the height of the reservoir column via an appropriate drainage port. Figure 1 shows also the two nozzles employed in this study. The 3 mm nozzle was made from a plastic compound which was cast in a precision-made mold and later machined to final dimensions. The 1.1 mm nozzle was machined directly from a Plexiglas rod.

The jet flow was recorded photographically using the set up shown schematically in Fig. 2. The photographic equipment consisted of a Hasselblad 500EL/M view camera fitted with extension tube no. 21 for detailed close-up shots, a Sunpak Model 320 photoflash and a 45 cm \times 75 cm section of translucent glass for diffusing the light from the flash. As shown in Fig. 2, the jet was positioned between light source and camera. The proper combinations of f-stop and shutter speed (in total darkness at "full" flash power), determined after a number of trials, are reported here in Table I.

To provide a reasonable range of fluid properties, this study was based on three different fluids:

- I. distilled water
- II. glycerol in water solution, 30% by volume
- III. glycerol in water solution, 70% by volume

The physical properties of the three fluids are reported in Table II. For each of the three fluids and the two nozzles, four different jet velocities ranging from 2 m/s to 20 m/s were observed. Thus, a total of 24 jets were observed and recorded.

III. The Characteristic Wavelength

The domain covered by the present study is shown on the Weber number-Reynolds number chart of Fig. 3. The following definitions apply,

$$We = \frac{\rho V^2 D}{\sigma}, \quad Re = \frac{\rho V D}{\mu} \quad (1,2)$$

where ρ , V , D , σ , and μ are, respectively, the jet density, velocity, diameter, surface tension (in contact with air), and viscosity.

As illustrated in Fig. 2, a and b denote the extremities of the photographed portion of the jet. The complete photographic record is available in a thesis written by Stockman ²⁰. Due to space limitations, in the present paper we analyze only a representative sample of this record.

Three photographs of the fast capillary jet flow are shown in Figs. 4(a), 5(a), and 6(a). Each photograph corresponds to one of the three different liquids used in this study. It is useful to take a close look at the shape (contour) of the photographed jets and in this way to recognize the large-scale meandering path followed by the jet. As the jet fluid viscosity increases from Fig. 4(a) to Fig. 6(a), the sharpness of the meandering path is enhanced to the point where, in Fig. 6(a), the sinusoidal contour of the jet is illustrated with amazing clarity.

The central objective of our study was to document in quantitative terms the meandering shape of fast capillary jets. To meet this objective, the jet contours were subjected to a wavelength analysis. In each case, the jet contour was projected (enlarged) on a screen and traced by hand on paper.

This operation produced two waveforms, one for the upper edge of the jet column and another for the lower edge. The waveforms were then digitized and fed into a computer program which calculated their Fourier transforms and determined the respective power spectra and cross correlation functions.

In order to learn how the characteristic wavelength varies with position along the jet, each photographed contour was divided into a number of segments [for example, 3 segments for the jet column shown in Fig. 4(a)]. Each segment was analyzed, and the results are presented in Figs. 4-6 as power spectra with λ/D on the abscissa and P^* on the ordinate. P^* is defined by

$$P^* = \frac{1}{D^4} \lim_{T \rightarrow \infty} \frac{1}{T} \int_0^T |X(f)|^2 dt \quad (3)$$

$$X(f) = \int_{-\infty}^{\infty} x(t) e^{-j\omega t} dt \quad (4)$$

where $x(t)$ is the contour waveform, $\omega = 2\pi f$, $f = V/\lambda$, and T is the sample length.

Figures 4(b)-4(d) demonstrate that, regardless of longitudinal position along the jet axis, the upper and lower waveforms have a single (narrow) band of wavelengths which dominate the power spectrum. In this study we refer to the predominant wavelength (λ corresponding to maximum P^*) as the meander wavelength λ_{\max} . Figures 4(b)-4(d) show also that the upper and lower waveforms have the same meander wavelength and, in all cases, the meander wavelength scales with the jet diameter. Furthermore, the upper and lower waveforms are in phase: this conclusion follows from the cross correlation function

$$r^* = \frac{1}{D^2} \lim_{T \rightarrow \infty} \frac{1}{T} \int_0^T x(t) y(t+\tau) dt \quad (5)$$

where $x(t)$ and $y(t)$ are the two waveforms, and τ is the predetermined phase shift (lag) between the two waveforms. As shown in Figure 4(e) the cross correlation function r^* reaches its peak value at zero lag, which indicates that the upper and lower waves are in phase. In conclusion, the flow regime documented in this study is not axisymmetric (varicose), but one which is characterized by a large-scale sinuous shape of wavelength λ_{\max} .

Similar conclusions regarding the existence of a characteristic meander wavelength emerge from the analysis of Figs. 5(a) and 6(a). Due to space limitations, only two samples are reported here as Figs. 5(b) and 6(b) while the complete record of the wavelength analysis may be found in Ref. 20.

Figure 7 shows a summary of the λ_{\max} measurements yielded by the present study. The plotted λ_{\max} represents the average over the given x-segment, however, in reality the meander wavelength is continuous in x .

IV. Discussion of experimental results

A theoretical interpretation of the present results is possible based on both the theory of hydrodynamic stability and the buckling theory of fluid columns. Batchelor and Gill ²¹ considered the linear stability problem associated with an inviscid round jet discharging into a quiescent fluid. They showed that sufficiently far downstream from the nozzle the jet is least stable to a temporal nonaxisymmetric ("sinuous" ²¹) disturbance whose axial wavelength is larger than several times the jet diameter. Similar conclusions were reached by Mattingly and Chang ²² who treated the linear stability of spatial disturbances imposed on the same jet configuration. In addition, Mattingly and Chang ²² studied the natural instability of the jet in the laboratory, and reported excellent agreement between experimental measurements and theoretical stability predictions. The same problem and conclusions were discussed in a most recent study by Lopez and Kurzweg ²³.

The connection between the nonaxisymmetric shape and fast capillary jets and the least stable disturbance predicted in Refs. 21-23 was recognized by Hoyt and Taylor ²⁴. Based on photographs similar to the ones obtained in the present study, Hoyt and Taylor ²⁴ were able to identify a visible axial wavelength of what is clearly a nonaxisymmetric jet shape. In Fig. 10 of their study, Hoyt and Taylor ²⁴ report that the visible axial wavelength increases exponentially in the downstream direction, much in the same manner as λ_{\max} of fluids I and II considered in the present study (Fig. 7). Inspired by the existing theoretical work of Batchelor and Gill ²¹ and Mattingly and Chang ²², Hoyt and Taylor ²⁴ interpreted their two-dimensional photographic record as a helical (three-dimensional) instability with long axial wavelength, as predicted by stability theory.

In a more recent experimental report, Freeman and Tavlarides²⁵ showed that when a liquid jet is suspended in a confluent stream, the jet develops a nonaxisymmetric shape when the relative velocity between jet and stream reaches a high enough value. Figures 2 and 3(a) published by Freeman and Tavlarides²⁵

show a sinuous contour whose ratio (axial wavelength)/(diameter) appear to be nearly identical to the ratio visible in Fig. 6(a) of the present study. Specifically, averaging over three complete wavelengths visible in Fig. 2 of Ref. 25 we obtain $\lambda_{\max}/D \approx 1.67$. Also, averaging over four complete wavelengths visible in Fig. 3(a) of Ref. 25 we estimate $\lambda_{\max}/D \approx 1.47$. Note that these two values of λ_{\max}/D , 1.67 and 1.47, fall right in the middle of the narrow band of characteristic wavelengths revealed by the power spectra of Figs. 6(b) - 6(e) in the present study.

To summarize, classical hydrodynamic stability arguments predict correctly the instability of the jet column to nonaxisymmetric disturbances, as well as the scale of the axial wavelength of such disturbances. However, there is one additional result which now has been documented by three independent experiments (Refs. 24,25 and the present study) which is not predicted by existing hydrodynamic stability analyses. This additional result is the tendency of the nonaxisymmetric wave to show a λ_{\max}/D value which approaches 1.5 in a region close enough to the nozzle where, as discussed by Hoyt and Taylor²⁴, the nonaxisymmetric disturbance has not had time to be amplified due to the form drag interaction between the liquid jet and the ambient air.

Insight into the origins of this additional feature is offered by the buckling of fluid columns²⁶⁻³¹. It is worth noting that as a theoretical viewpoint in fluid mechanics, the buckling theory is much newer than hydrodynamic stability theory. The novelty of the concept of fluid column buckling

may indeed be responsible for the early interpretation of nonaxisymmetric disturbances in fast capillary jets as helical. In fact, the experimental record available for this interpretation is exclusively two-dimensional and, as such, the same record can be interpreted as evidence of local buckling in a plane determined randomly by the presence of random disturbances at the air interface.

This alternative interpretation is recommended strongly by the first observations of fast capillary jet flow, in particular by Weber's¹⁵ Figs. 1(b), 1(d) and 1(e). In these early photographs the lateral deformation of the liquid column has a local (nonperiodic) character, however, the wavelength of this deformation is always a characteristic multiple of the jet thickness. The same effect is visible in Fig. 6(a) of the present study, where entire sections of the jet appear to be undisturbed while other segments show the characteristic wave λ_{\max} .

Theoretically, it has been shown that a column of viscous fluid can buckle in a way similar to rods in axial compression^{26,27}, however, the wavelength of the buckled shape depends solely on the wavelength of the initial lateral disturbance. On the other hand, for a column of inviscid fluid it is found that the buckling wavelength always scales with the column diameter^{30,31},

, $\lambda/D = \pi/2 = 1.57$. This prediction can then serve as explanation for the observed axial wavelength of incipient nonaxisymmetric deformations in fast capillary columns.

Figure 8 compares graphically the theoretical buckling shape of a round jet^{30,31} with a close-up view of the jet photographed in Fig. 6(a). The similarity of the two waveforms is striking.

A strong indication that the buckling theory of inviscid jets accounts correctly for the meandering wavelength documented in this study is that the wave of Fig. 6(a) agrees very well with the wave photographed by Freeman and Tavlarides²⁵. Note that for fluid III the Reynolds number is in the range 10 - 100 and the Weber number in the range $10^3 - 10^4$; these ranges are quite different from Ref. 25 where $Re \sim 10^3$ and $We \sim 14$. The fact that despite such discrepancies the photographed wavelengths agree with each other and with the buckling wavelength $\pi D/2$ supports the buckling theory very strongly. The key result of the buckling theory is that the buckling wavelength must depend only on D, in other words, it must be independent of V and physical properties. For the same reason, the fact that for fluids I and II λ_{max} increases with x is a reflection of the thickening of the air stream entrained by the liquid jet. Thus, sufficiently far downstream the liquid jet meanders according to the buckled shape of the surrounding (thicker) air stream.

A The connection between the nonaxisymmetric flow of fast jets and fluid buckling requires further study. Some have already expressed the view that fluid buckling may serve as origin for the turbulent motion of fluids³¹⁻³³. Along the same lines, it is interesting to note Lopez and Kurzweg's²³ early statement that the nonaxisymmetric instability of jet flow may actually account for "the breakdown phenomenon in boundary layer flow", hence, for the well-documented bursting process³⁴.

Acknowledgment. This research was conducted under the auspices of the Office of Naval Research. The experimental apparatus was constructed by Mr. Karl Rupp.

References

1. G. Bidone, Imprimerie Royal, Turin, 1-136 (1829).
2. E. Savart, Ann. Chem., 53, 337 (1833).
3. Lord Rayleigh, The Theory of Sound, (Dover, New York, 1945), ch. XX.
4. S. Chandrasekhar, Hydromechanic and Hydromagnetic Stability,
(Clarendon, Oxford 1961).
5. L. Crane, S. Birch, and P. McCormack, Brit. J. Appl. Phys., 15,
743 (1964).
6. R. Donnelly and W. Glaberson, Proc. Royal Soc., A290, 547 (1966).
7. M.C. Yuen, J. Fluid Mech., 33, 151 (1968).
8. A.H. Nayfeh, Phys. Fluids, 13, 841 (1970).
9. P. Lafrance, Phys. Fluids, 18, 428 (1975).
10. E.F. Goedde and M.C. Yuen, J. Fluid Mech., 40, 495 (1970).
11. D.F. Rutland and G.J. Jameson, J. Fluid Mech., 46, 267 (1971).
12. K.C. Chaudhary and L.G. Redekopp, J. Fluid Mech., 96, 257 (1980).
13. K.C. Chaudhary and T. Maxworthy, J. Fluid Mech., 96, 275 (1980).
14. K.C. Chaudhary and T. Maxworthy, J. Fluid Mech., 96, 287 (1980).
15. C. Weber, Z.A.M.M., 11, 136 (1931).
16. A. Haenlein, Forschung, 2, 139 (1931).
17. L. Prandtl, Essentials of Fluid Dynamics, (Blackie and Son, London,
1969), 325.
18. J.W. Hoyt, J.J. Taylor and C. Runge, J. Fluid Mech., 63, 635 (1974).
19. J.W. Hoyt and J.J. Taylor, Phys. Fluids, 20, S253 (1977).
20. M.G. Stockman, M.S. Thesis, University of Colorado, Boulder 1981.

21. G.K. Batchelor and A.E. Gill, J. Fluid Mech., 14, 529 (1962).
22. G.E. Mattingly and C.C. Chang, J. Fluid Mech., 65, 541 (1974).
23. J.L. Lopez and U.H. Kurzweg, Phys. Fluids, 20, 860 (1977).
24. J.W. Hoyt and J.J. Taylor, J. Fluid Mech., 83, 119 (1977).
25. R.W. Freeman and L.L. Tavlarides, Phys. Fluids, 22, 782 (1979).
26. J.D. Buckmaster, A. Nachman, and L. Ting, J. Fluid Mech., 69, 1 (1975).
27. J.D. Buckmaster and A. Nachman, Q.J. Mech. Appl. Math., 31, 157 (1978).
28. S.M. Suleiman and B.R. Munson, Phys. Fluids, 24, 1 (1981).
29. B.R. Munson, Phys. Fluids, 24, 1780 (1981).
30. A. Bejan, Lett. Heat Mass Transfer, 8, 187 (1981).
31. A. Bejan, Phys. Fluids, 24, 1764 (1981).
32. B.R. Munson, Phys. Fluids, 24, 1766 (1981).
33. J.O. Cruickshank, Ph.D. Thesis, Iowa State University, Ames 1980.
34. H.T. Kim, S.J. Kline, and W.C. Reynolds, J. Fluid Mech., 50, 133 (1971).

Table I

Proper exposure settings for photography
in total darkness at "full" flash power

Film Type	f-stop	Shutter Speed
Kodak EPR 120	4	1/30 sec
Kodak PXP 120	5.6	1/30 sec

Table II

Physical properties of the working fluids

Fluid	Density [g/cm ³]	Viscosity [cS]	Surface Tension [g/s ²]
I. Distilled Water (18°C)	1	1	73
II. Glycerol-Water, 30% by volume (20°C)	1.18	17	68
III. Glycerol-Water, 70% by volume (20°C)	1.24	333.6	64.5

List of Captions

Fig. 1 Schematic of experimental apparatus and nozzle design.

Fig. 2 Photographic arrangement, and the coordinates of the photographed jet segment.

Fig. 3 Weber number - Reynolds number domain covered by the present experiments.

Fig. 4 Meandering jet of fluid I, $D = 1.1$ mm, $V = 17$ m/s, $a = 0$ mm, $b = 165$ mm.

a) photograph

b) spectral density of segment 51mm-71mm downstream from nozzle

c) spectral density of segment 71mm-91mm downstream from nozzle

d) spectral density of segment 91mm-111mm downstream from nozzle

e) cross correlation function of segment 51mm-71mm downstream from nozzle.

in Figs. 4(b) - 4(e) the upper and lower waveforms are labeled \triangle and \circ , respectively.

Fig. 5 Meandering jet of fluid II, $D = 3$ mm, $V = 11.2$ m/s, $a = 146$ mm, $b = 324$ mm.

a) photograph

b) spectral density of segment 168 mm - 183 mm downstream from nozzle; the upper and lower waveforms are labeled \triangle and \circ , respectively.

Fig. 6 Meandering jet of fluid III, $D = 3$ mm, $V = 15.2$ m/s, $a = 140$ mm, $b = 305$ mm.

a) photograph

b) spectral density of segment 267 mm - 278 mm downstream from nozzle; the upper and lower waveforms are labeled \triangle and \circ , respectively.

Fig. 7 The measured meandering or buckling wavelength vs. longitudinal position along the jet.

Fig. 8 The theoretical ^{30,31} shape of a buckled inviscid jet vis-à-vis a close-up of Fig. 6(a).

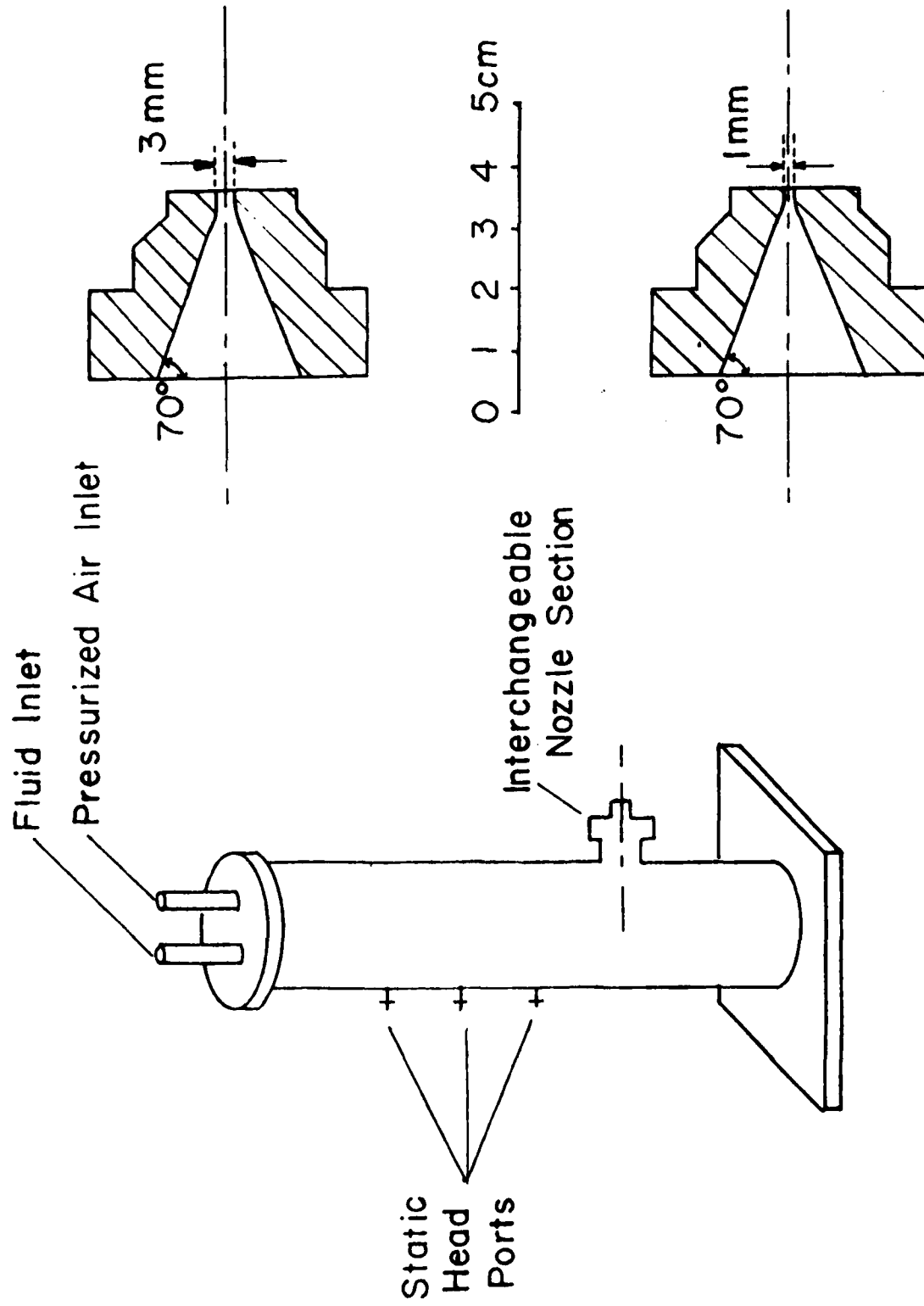


Fig. 1

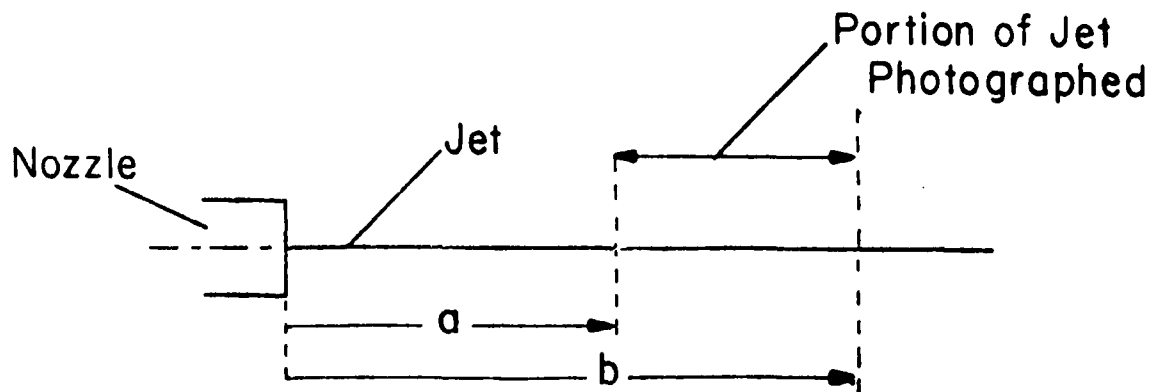
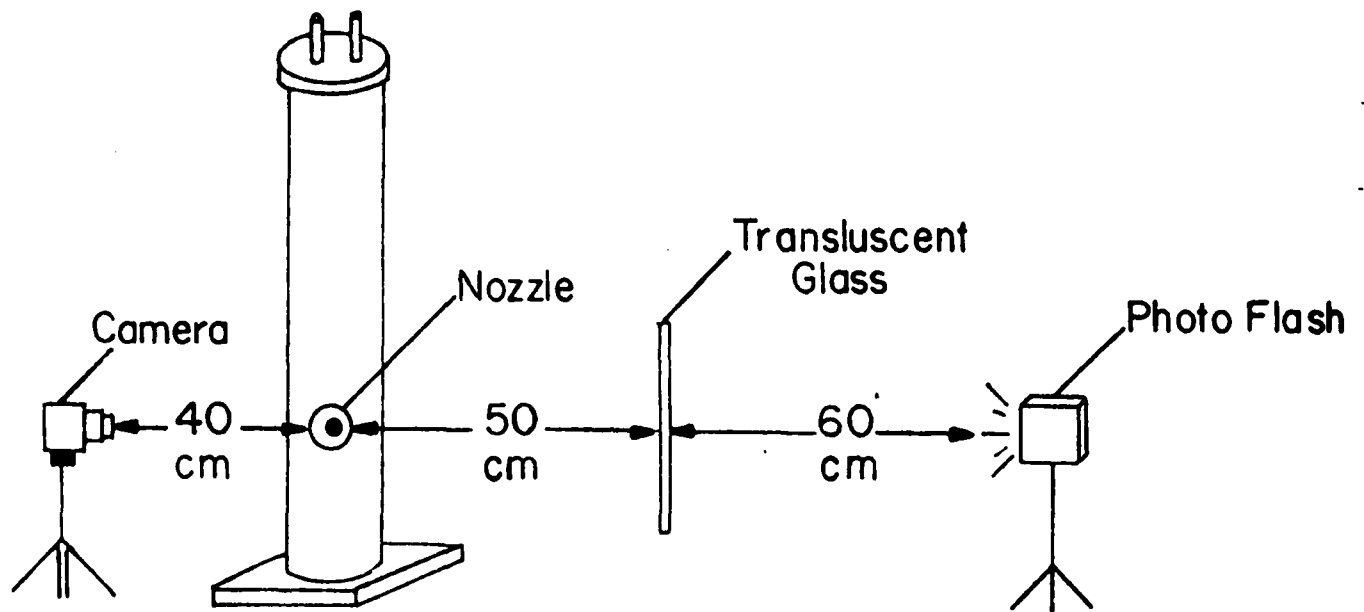


Fig. 2

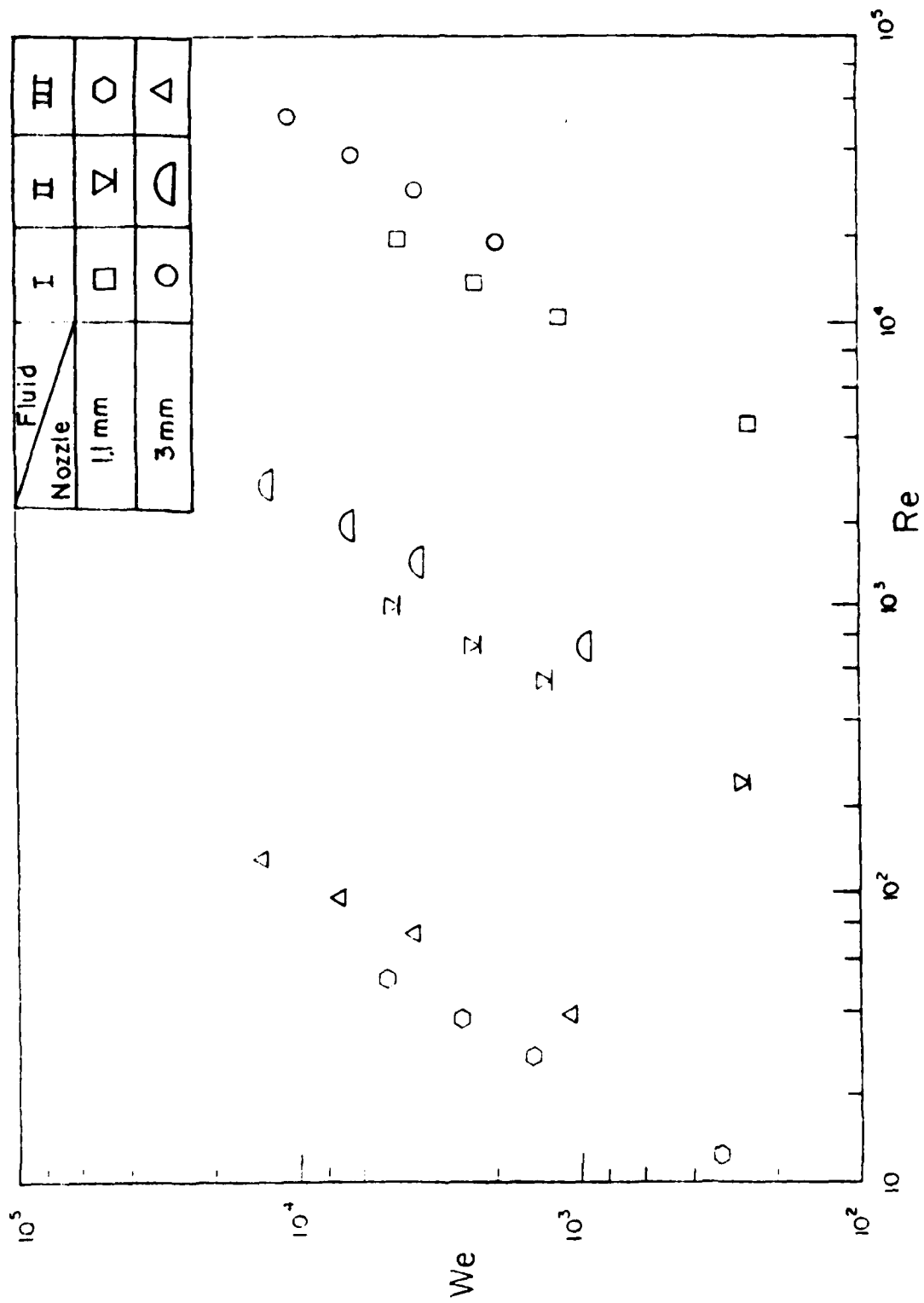
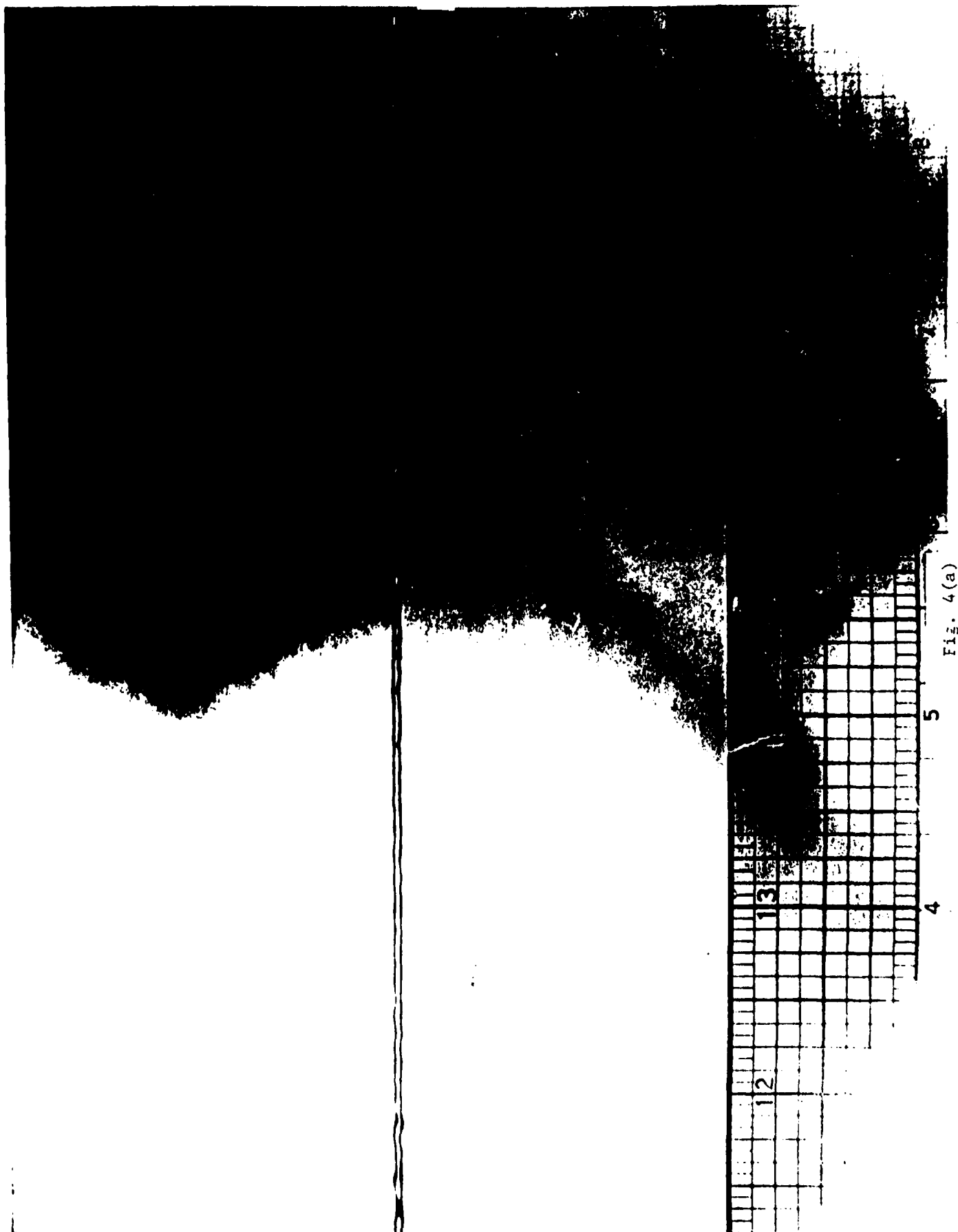


Fig. 3



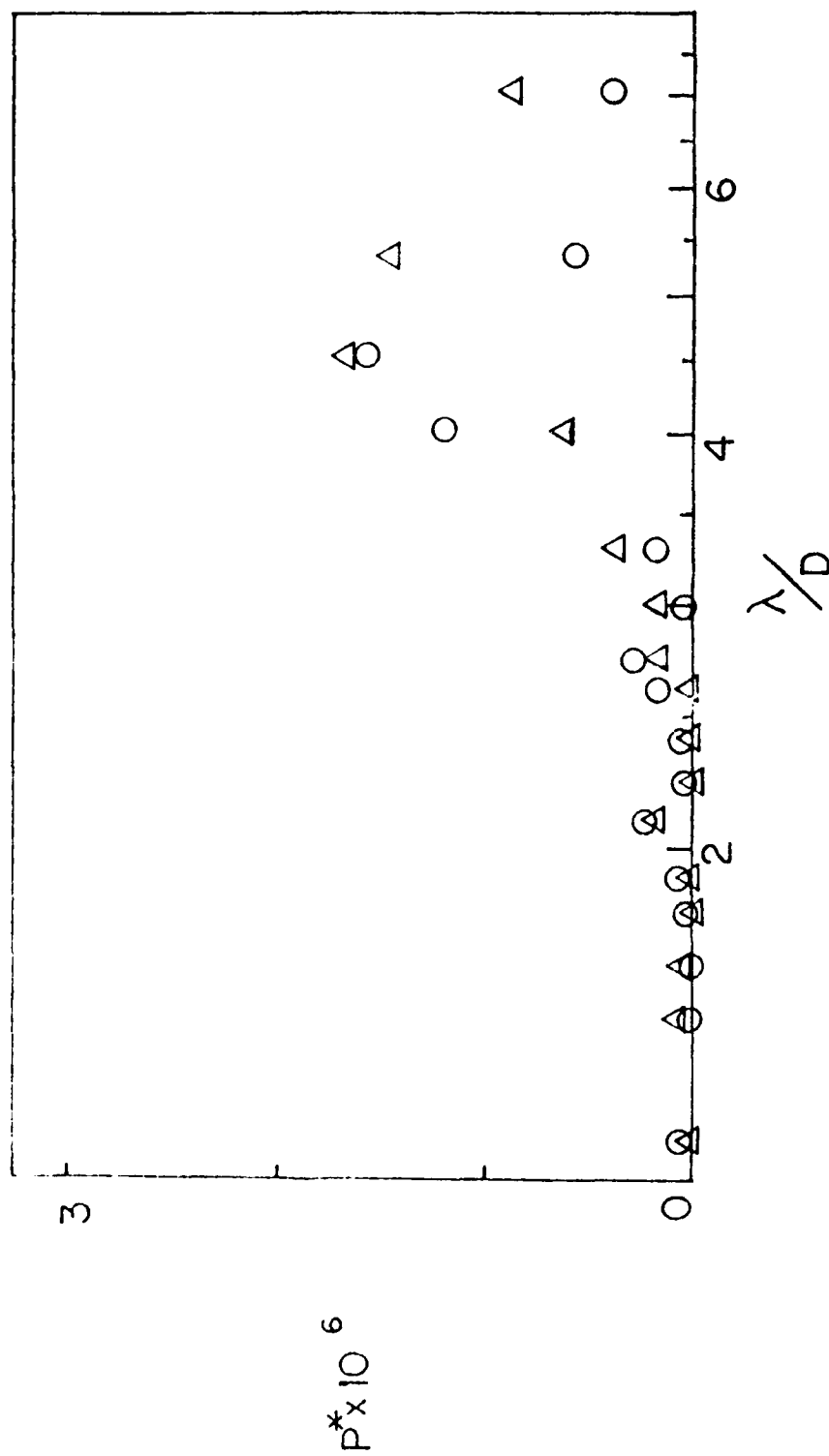


Fig. 4(b)

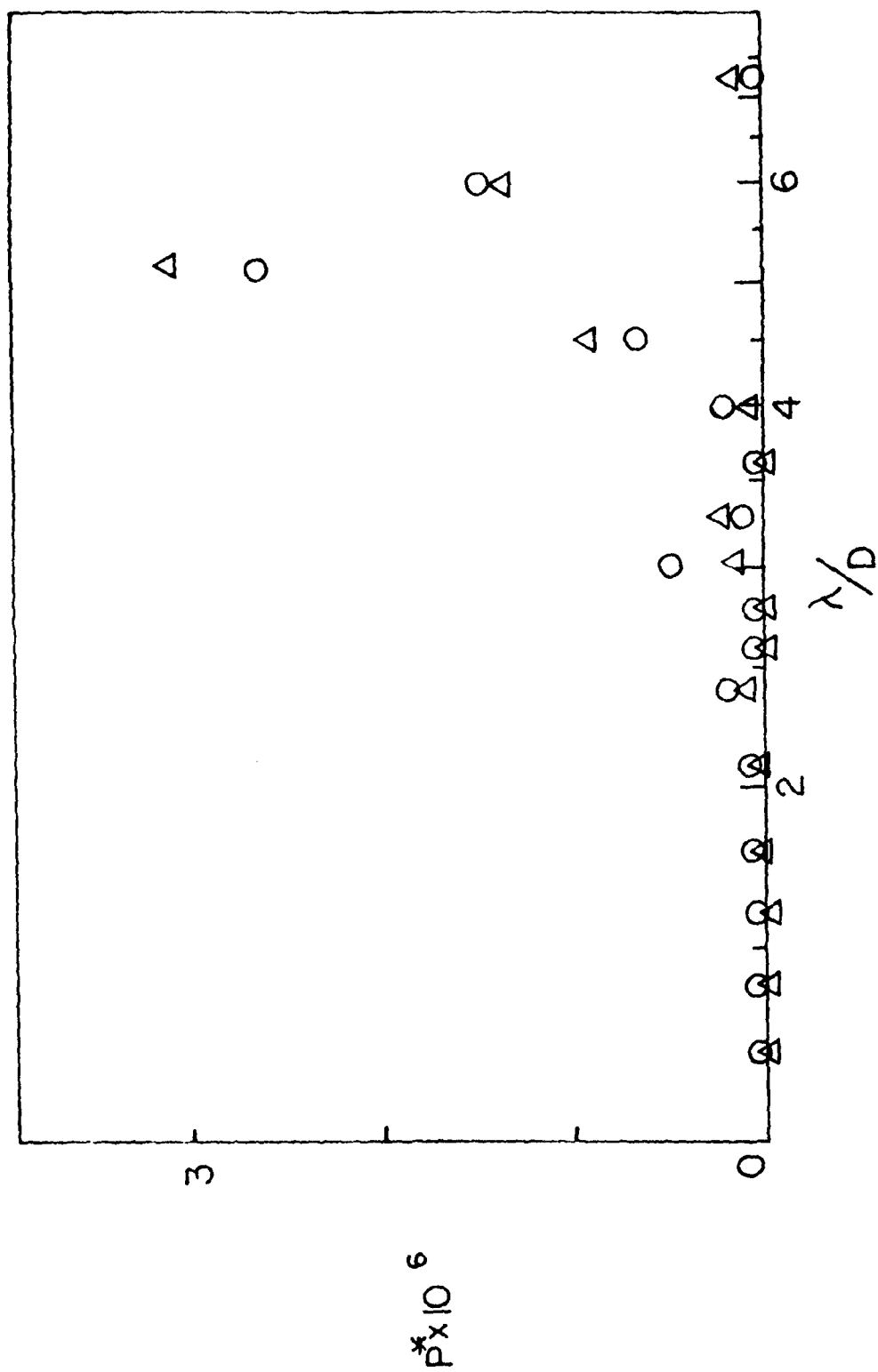


Fig. 4(c)

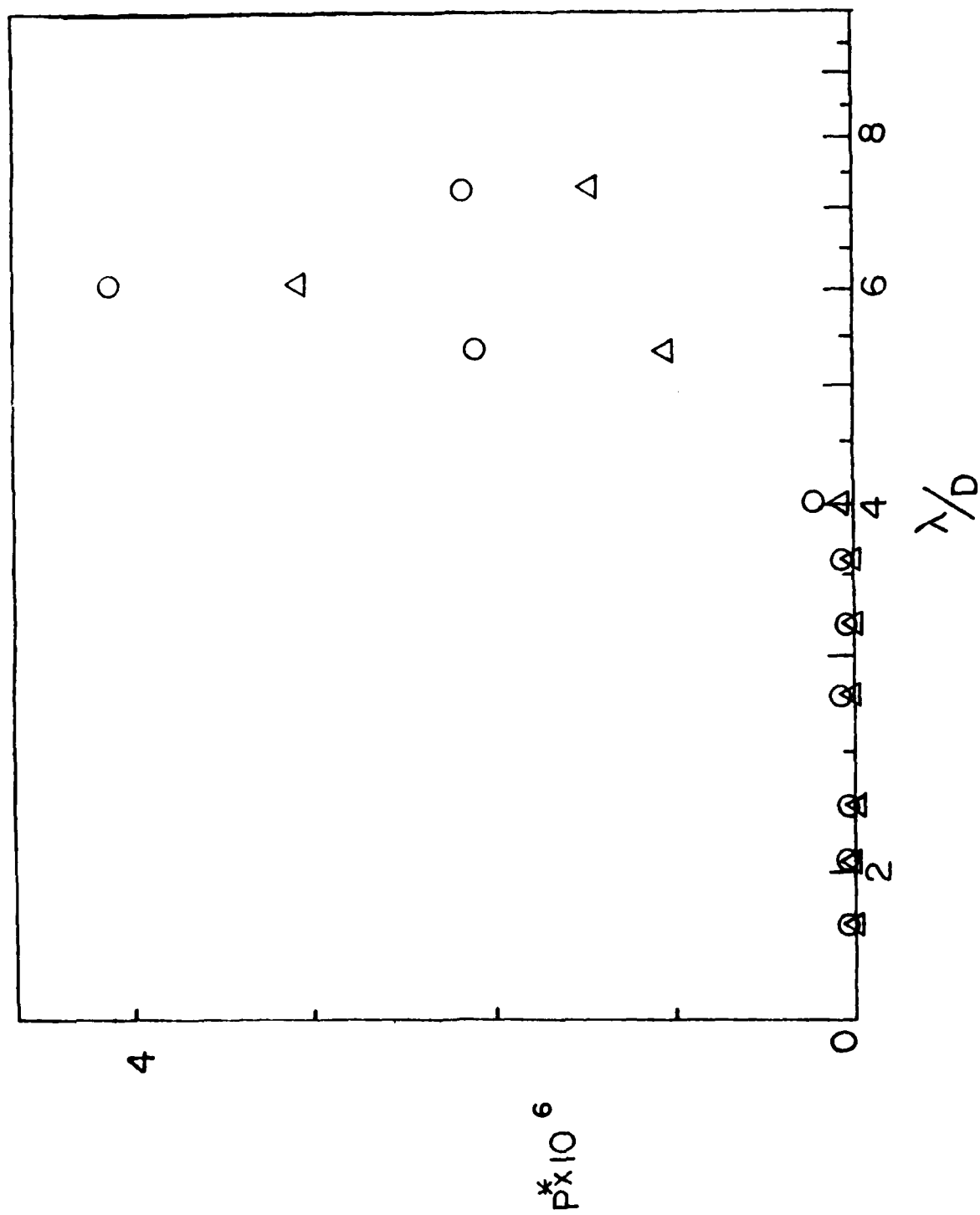


Fig. 4(d)

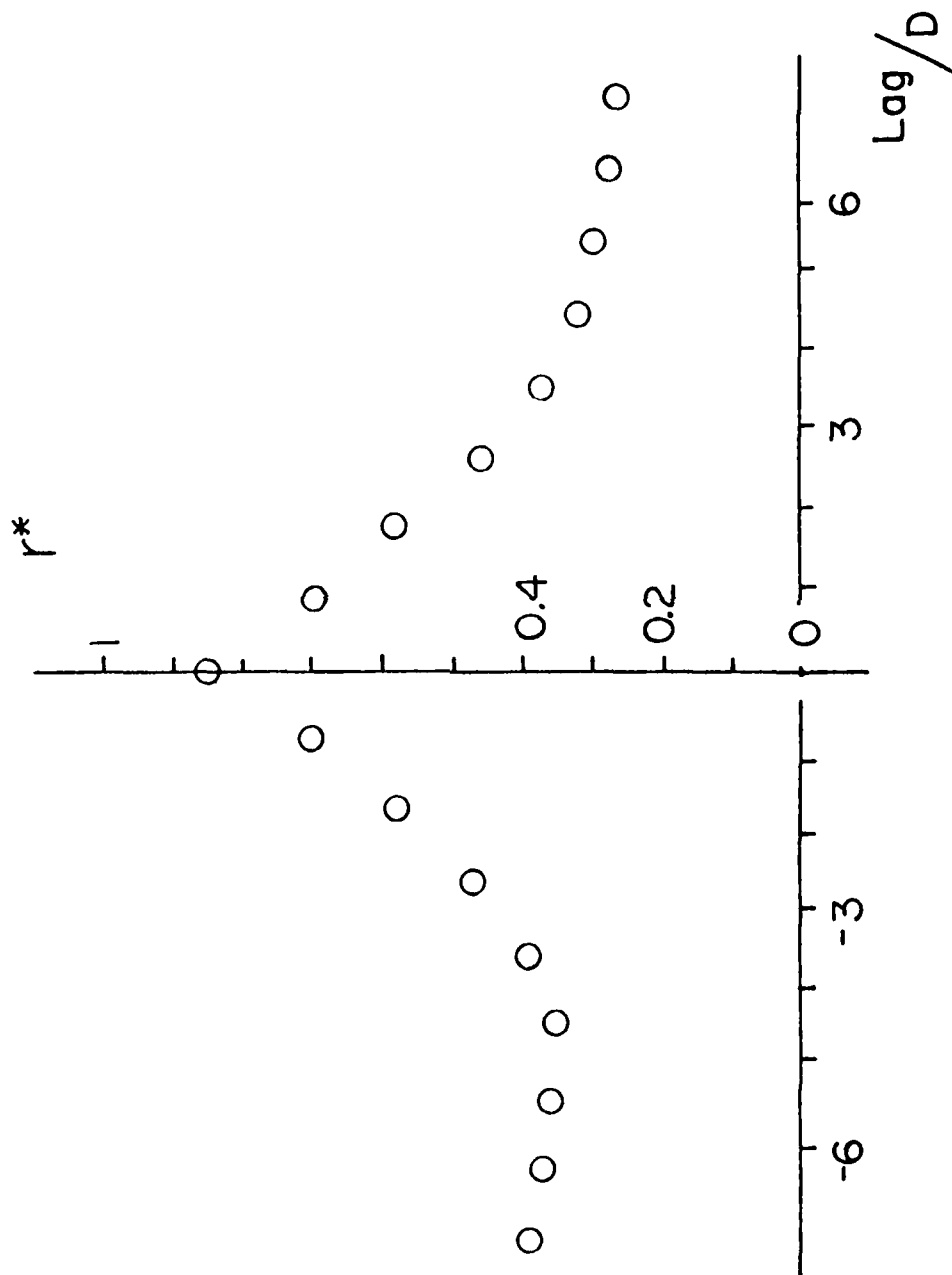
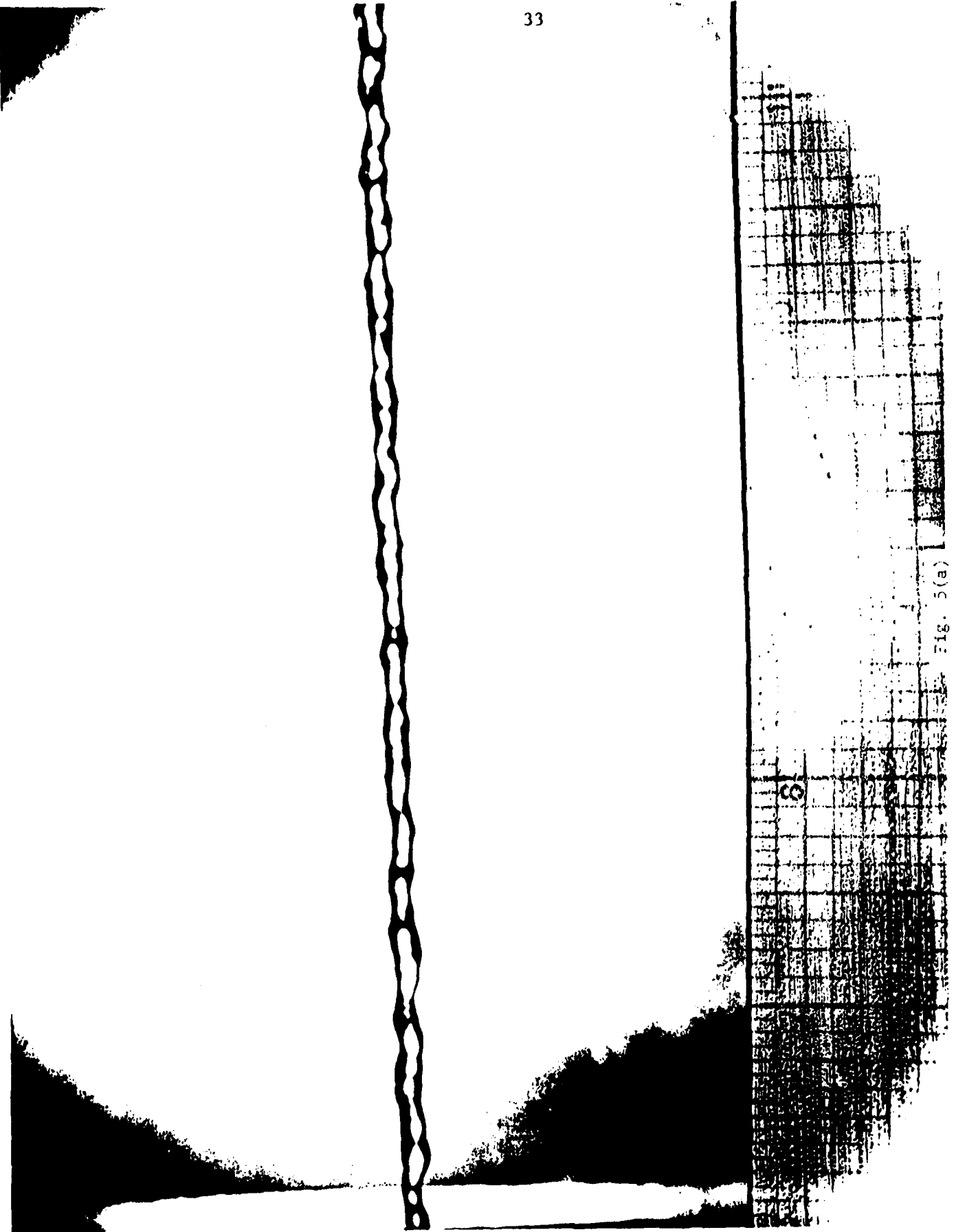


Fig. 4(e)



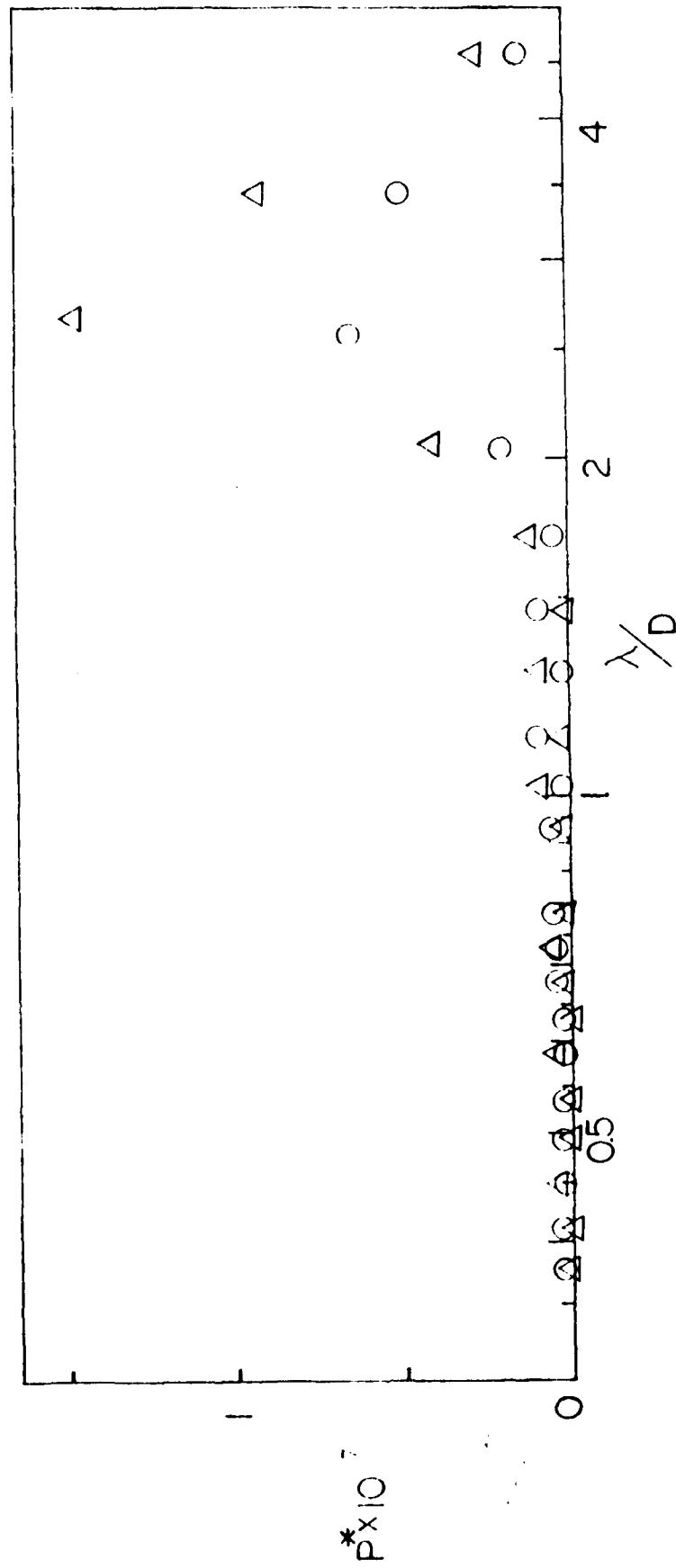


Fig. 5(b)



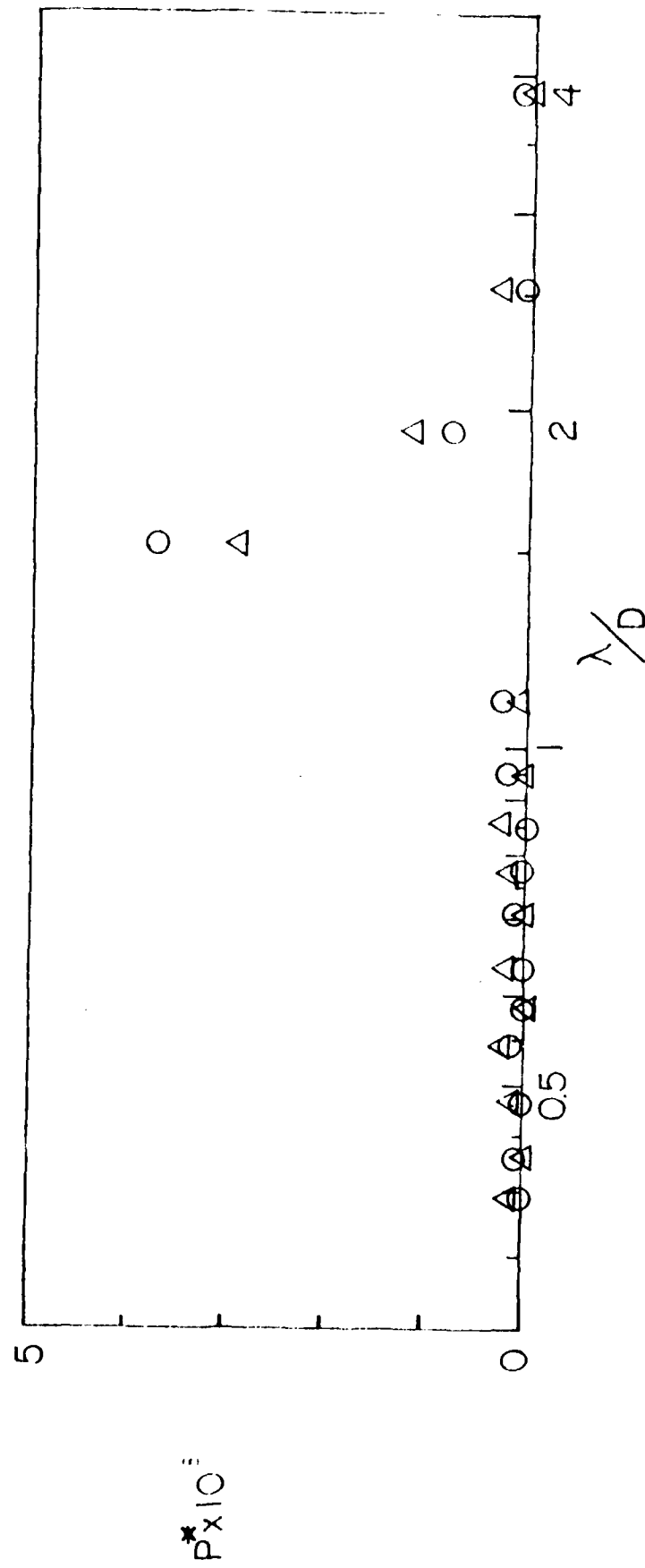


Fig. 6(b)

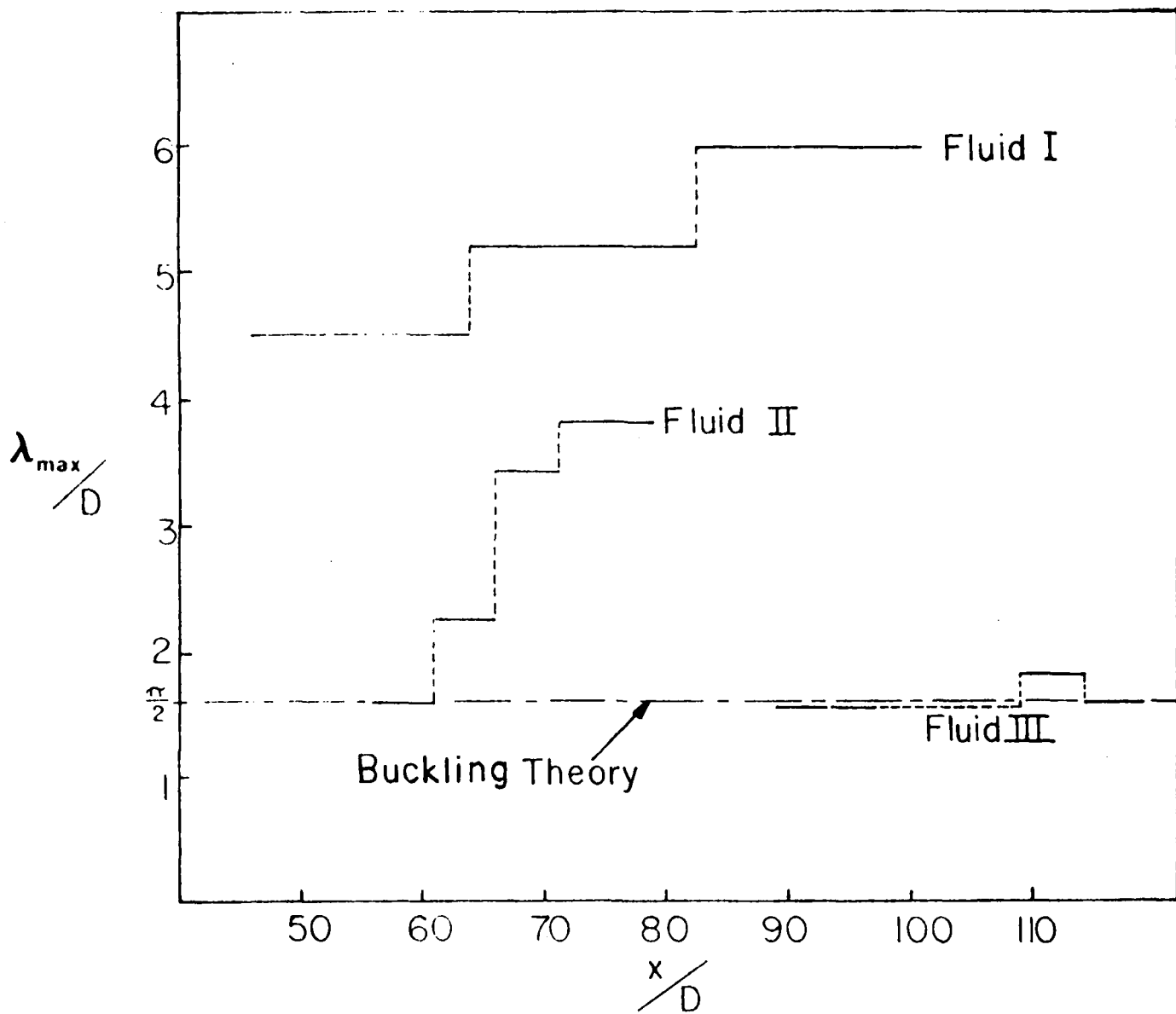


Fig. 7

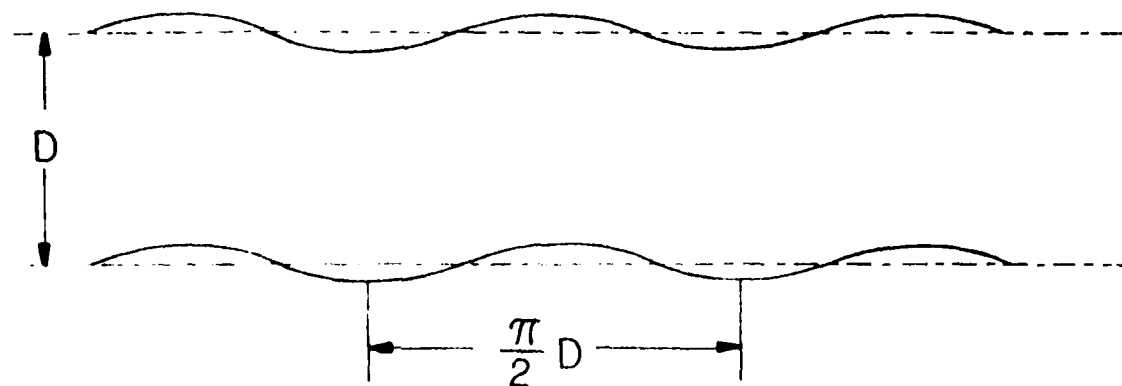


Fig. 8

SECTION 5

Theoretical Explanation for the Incipient
Formation of Meanders in Straight Rivers*

by

Adrian Bejan
Department of Mechanical Engineering
University of Colorado, Campus Box 427
Boulder, Colorado 80309 USA

Abstract

This paper advances a theoretical explanation for the lateral periodicity and geometric similarity of meanders observed in rivers of many sizes. Invoking the static equilibrium of a straight river bed, it is shown analytically that the equilibrium shape of the bed is a unique sinusoid. The theoretical wavelength of the sinusoidal shape is proportional to the width of the river, in agreement with visual observations of rivers of all sizes.

*published in Geophysical Research Letters, Vol. 9, August 1982, pp.831-834.

1. The Geometric Similarity of River Meanders

The sinuous course of rivers is one of the most visible and widespread phenomena in nature. We see meanders not only in rivers of all sizes, but also in rivulets (tricklings on a solid surface; Tanner 1960, 1962, Gorycki 1973a, b), in ocean currents such as the Gulf Stream (Von Arx 1952, Stommel 1954), in melt water streams carved in glacier ice (Leopold and Wolman 1960), and, practically, in all inviscid jet flows (e.g. the meandering of turbulent jets, Crow and Champagne 1971, or the instantaneous sinuous shape of turbulent buoyant plumes, Turner 1979).

The most basic feature of the meander phenomenon is the proportionality between meander wavelength λ and stream width W (Leopold and Wolman 1960). As concluded in a recent review article (Callander 1978), significant theoretical progress has been made in the direction of explaining the occurrence of meanders and accounting for measured meander parameters. The theories developed over the past thirty years have in common the thinking framework offered by the Theory of Hydrodynamic Stability: according to this approach, one analyzes the stability or instability of sinusoidal waves (disturbances) superimposed on the straight river flow. As summarized by Parker (1976), consideration of gravity waves led Werner (1951) to the conclusion that $\lambda/W \sim 2F$, where F is the flow Froude number. Hansen (1967) posed the linearized stability problem associated with a meandering (sinusoidal) disturbance and found $\lambda/H = 7 F^2/S$, where H is the river depth and S is the dip angle of the river bed. Anderson (1967) analyzed transverse oscillations and obtained $\lambda/W = \text{constant} \times (F H/W)^{1/2}$.

A number of improved models of hydrodynamic stability have been reported more recently, for example, Callander (1969), Sukegawa (1970), Hayashi (1974), Engelund and Skovgaard (1973) and Parker (1976). Callander (1969) considered a two-dimensional model and assumed that the pressure and shear stress vary linearly in the vertical direction. He assumed also that the bed shear stress and the rate of transport of bed load do not depend on river depth and are functions of the water velocity only. The results of the stability analysis showed that the initial growth rate of the assumed disturbances should have a maximum and that the wavelength corresponding to this maximum agrees roughly with observations. Parker's (1976) analysis was similar but more general. For the maximum initial growth rate Parker obtained $\lambda/(WH)^{1/2} = 2\psi(\pi F/C_0)^{1/2}$, where C_0 is the drag coefficient and ψ a coefficient associated with the particular constitutive equations used. Sukegawa (1970) assumed constant drag coefficients and a rate of transport of bed load as a function of the bed shear stress. As criterion for instability, Sukegawa used a critical value of the ratio of the amplitude of the disturbance to the bed divided by the amplitude of the surface disturbance.

The stability problem in a three-dimensional flow model was considered by Engelund and Skovgaard (1973). They found that instability occurs for a range of horizontal wavelengths, however, they did not compare their results with experimental observations. Hayashi's (1974) analysis relied on the assumption of irrotational flow and that the bed load transport rate depends on the velocity at $x - \delta$, where δ is a short distance by which the local transport lags behind the local force on the bed. One of Hayashi's findings is that for subcritical flow ($F < 1$) the maximum disturbance amplification rate corresponds to $L/(WH)^{1/2} = 72 F^{1/2}$; this result is similar to the conclusions of Anderson (1967) and Parker (1976), as summarized in Table 1.

The chief contribution of the theoretical research reviewed above and, in greater detail, in Callander (1978) is to have shown that the bed of a channel with straight banks is unstable: since the bed is composed of moving sediment, the amplitude of a certain class of disturbances is likely to grow the fastest. In addition, this research predicted correctly the direction of migration and the downstream wave speed of meanders. These conclusions are important and will be adopted without debate in the theory developed in this paper. However, the chief limitation of the existing theories is also important: note should be made of the fact that the ratio λ/W predicted by hydrodynamic stability considerations (Table 1) does not have a characteristic (unique) range of values, contrary to the statistical evidence compiled over natural streams of widely varying sizes (Leopold and Wolman 1960). This limitation is accepted from the start by every stability analyst who recognizes the existence of disturbances of every wavelength and then tries to identify which of these disturbances will develop the most rapidly.

Inasmuch as the constancy of the ratio λ/W appears to be an intrinsic property of all streams, the stability theories explain the evolution (behavior) of existing meanders but not their origin.

The theory constructed in this paper addresses the question which has not yet been addressed, namely, why does a straight (undisturbed) river choose a sinuous shape of precise wavelength? Before presenting the theoretical answer to this fundamental question, the author finds it necessary to review a class of very useful experiments which shed light on the natural properties of the (river)-(flexible bed) system.

2. The Stream Plate Experiments

The original stream plate experiment was proposed by Tanner (1960) as a means of visualizing the natural tendency of streams to meander. The same technique was used in a comprehensive study by Gorycki (1973a). The experiment consists of a smooth plane surface which supports a water jet flow issuing from a nozzle tangent to the surface. Thus, the stream plate experiment is the laboratory version of water tricklings commonly observed on shower walls and car windshields. The water columns generated in this fashion meander much in the same way as rivers do. However, there is one important advantage to this experiment, namely, the opportunity to observe the incipient phase of the meandering process in a straight jet.

Of interest here are Tanner's and Gorycki's observations, and the clever mechanical analog visualized by Gorycki to simulate river meandering. First, the stream plate visualization of the meander formation process is strong evidence that the meander is a property of the stream; this property is independent of the effects of sediment. In comparing various stream plate experiments, Gorycki (1973b) argues further that plate roughness is not necessary for meander formation.

The experiments also showed (Tanner 1962) that meandering is independent of the secondary flow or disturbances which may be present in the nozzle. This conclusion is strengthened by the statement made by Schumm and Khan (1972) who observed meanders made in the laboratory under straight entrance conditions: "... a perturbation or disturbance of the flow may not be an essential cause of meandering" (Gorycki 1973a, p. 178). The fact that initial disturbances are not essential to meandering should be kept in mind: this fact is partly responsible for the drastic departure the present theory will make relative to the classical path of Hydrodynamic Stability.

Gorycki presented also a mechanical analog of the river meandering mechanism: he held a slender piece of elastic (a slender cylindrical column of rubber) between two parallel pieces of glass. He then moved the glass pieces relative to one another, in the direction parallel to the cylinder axis. As a result, the piece of elastic assumed a shape which resembles very closely that of a meandering river or that of a meandering stream in a stream plate experiment. At the end of his description of this mechanical analog, Gorycki expressed his hope "that a mathematical model could be designed to quantify this mechanism".

It is shown in the next section that the mechanism responsible for elastic meandering is also responsible for river meandering. In Mechanical Engineering, which is the present author's education, the sinusoidal shape of the elastic column has been explained as the buckling property of slender spaces in longitudinal compression. The buckling of slender columns represents an important and voluminous chapter in the centuries-old discipline of Strength of Materials (Den Hartog, 1961). The theoretical basis for this chapter was established by Euler, who pointed out that in order for a slender space to buckle into an equilibrium sinusoidal shape it must satisfy only two conditions (Love 1927):

- (i) the slender space must be in a state of axial (longitudinal) compression.
- (ii) the material which fills the space must be such that if the space is subjected to a separate bending test of prescribed curvature, then the space develops in its cross-section a resistive bending moment (couple) which is proportional to the local curvature.

The piece of elastic described by Gorycki satisfies the above conditions. But it is important to keep in mind that conditions (i) and (ii) do not refer to a specific material such as an elastic solid: they refer to a space (column) of finite size. The objective of the following analysis is to prove that the river and its bed, as a slender space, also satisfy conditions (i) and (ii) necessary for sinusoidal buckling.

3. The Static Equilibrium of a Straight River

Consider a straight, inviscid, river flow of uniform velocity V_o , density ρ , width W and depth H . The bed of the river is horizontal. In the stationary frame of reference of the bed, the river cross-section exhibits a uniform compressive stress $\rho V_o^2 + P_o(z)$, where P_o is the excess pressure

$$P_o(z) = \rho g (H - z) \quad (1)$$

and g is the gravitational acceleration. The resultant of this compressive stress, integrated over the river cross-section, is

$$C = \rho V_o^2 WH \left(1 + \frac{gH}{2V_o^2}\right). \quad (2)$$

Therefore, in the frame of reference of the bed, the straight river is a slender column in longitudinal compression. This means that condition (i) is satisfied. In order to see that the bed, as a duct, is in a state of longitudinal compression, the reader should think of a piece of garden hose through which the flowrate is high (turbulent). The hose is pushed axially by the reactive compressive force associated with the stream leaving through the open end. The same hose is pushed axially in the opposite direction by the impactive force associated with the stream entering it from the faucet.

As shown in Fig. 1, the static equilibrium of the bed requires two statements, one for translational equilibrium (obvious, $C \equiv C$) and the other for rotational equilibrium. The rotational equilibrium condition is made necessary by the fact that no straight river is ever "mathematically" straight, in other words, all straight rivers are subjected to an infinitesimally small couple CY due to the imperfect colinearity of the axial forces C . The rotational equilibrium condition is (Den Hartog 1961).

$$CY - M + M_o = 0 \quad (3)$$

where M is the couple acting over the river cross-section.

It is easy to show that the river column also satisfies condition (ii), or that a net couple M is present whenever the column $Y(X)$ is locally curved. Consider a separate bending test in which the river radius of curvature R_∞ is infinitely greater than the river width W (Fig. 2). The new velocity V and pressure distribution P in the cross-section can be determined immediately from Bernoulli's equation (Prandtl 1969)

$$\frac{1}{2} \rho V^2 + P = \frac{1}{2} \rho V_o^2 + P_o \quad (4)$$

combined with a local force balance in the radial direction y (Prandtl 1969),

$$\frac{\rho V^2}{R_\infty} = \frac{\partial P}{\partial y} \quad (5)$$

In the limit of vanishingly small curvature^{*}, $W/R_\infty \rightarrow 0$, we obtain

$$V = V_o \left(1 - \frac{y}{R_\infty}\right) \quad (6)$$

$$P = \rho V_o^2 \frac{y}{R_\infty} + \rho g (H - z). \quad (7)$$

A related result is that the free surface $z_f(y)$ acquires a slight tilt

$$z_f(y) = H + \frac{V_o^2 y}{g R_\infty} \quad (8)$$

Due to the slight tilt, the center of mass of the cross-section shifts from $y = 0$ to $y_o = V_o^2 W^2 / (12 g H R_\infty)$, where $y_o \ll W$.

According to the standard methods of mechanical engineering, the net bending moment M about the vertical line passing through the center of mass of the cross-section is

$$M = \int_{y=-W/2}^{y=W/2} \int_{z=0}^{z=z_f(y)} (\rho V^2 + P) (y - y_o) dz dy = - \frac{\rho V_o^2 H W^3}{8 R_\infty} \quad (9)$$

^{*} this is the same as the limit of zero meander amplitude; however, in this limit the meander wavelength can still be finite, as found in equation (13).

This result demonstrates that the river cross-section experiences a bending moment as soon as the river trajectory has curvature. Equation (9) proves that rivers also obey condition (ii) for sinusoidal buckling.

4. The Natural Sinusoidal Shape of Rivers

In the limit of infinitesimally small deviations from the rectilinear shape, the river curvature $1/R_\infty$ is equal to $-d^2Y/dX^2$. Based on this approximation and equation (9), the static equilibrium condition (3) becomes

$$CY + \frac{1}{8} \rho V_o^2 HW^3 Y'' + M_o = 0 \quad (10)$$

The general equilibrium shape of the river bed follows from equation (10),

$$Y(X) = \frac{M_o}{C} [\cos(2\pi \frac{X}{\lambda}) - 1], \quad (11)$$

where the wavelength λ has a precise value given by

$$\frac{\lambda}{W} = \frac{\pi}{[2 + gH/V_o^2]^{1/2}} \quad (12)$$

For shallow rivers and for stream plate simulations ($gH/V_o^2 \ll 1$) we find

$$\frac{\lambda}{W} = \frac{\pi}{\sqrt{2}} = 2.22, \text{ universal constant} \quad (13)$$

In conclusion, the natural (equilibrium) shape of the river bed is a sinusoid whose wavelength is a precise multiple of the river width. The amplitude of this shape is unknown (infinitely small), because the analysis leading to equation (12) invoked the static equilibrium of a straight river. It is well known, however, that the equilibrium of a nearly straight river bed is unstable (cf. Hydrodynamic Stability Theory, Section 1) and that the highly regular, sinuous, shape determined here is destined to grow in amplitude.

5. Conclusion

The fundamental contribution of this theoretical argument is the prediction of a universal proportionality between meander wavelength and river width, equations (12, 13). This prediction is supported strongly by observations of meander formation in straight rivers and in stream plate experiments. Attention is drawn first to the stream plate experiments (Gorycki 1973a, p. 179, Figs. 3,8,9,10,13) which conclusively show "that the spacing between the sinuous curves or point bars in straight streams is approximately two to three times the stream width", as in equation (13). Similar values of λ/W in straight rivers were reported by numerous field studies^{*}, for example, in Leopold, Wolman and Miller (1964), Leopold and Wolman (1970, Fig. 7.8) and Dury (1964, Figs. 26,28). A ratio λ/W between 2 and 3 appears to be a universal feature of all straight streams. Keller (1972, p. 1534) showed that only in the late stages of meander development λ/W reaches values in the range 5-7, whereas during development the ratio λ/W is in the range 3 - 5.

Table 2 shows a summary of experimental observations next to the constant ratio λ/W predicted by the present theory of river buckling. The present theory agrees with observations made in straight or nearly straight rivers, which conform to the type of system selected here for analysis in section 2. Table 2 shows also that, as time passes, the ratio λ/W increases from the initial theoretical value (2.22) to the natural (long-history) value of approximately 10. Thus, the present theory offers a concise explanation for the origin of meanders in straight rivers, however, it does not account for the geometry of meanders in their late stages of development.

Acknowledgement. This research was supported by the U.S. Office of Naval Research, under Contract No. N00014-79-C-0006.

^{*} This literature is reviewed in greater detail in Gorycki (1973a).

References

- Anderson, A. G., On the development of stream meanders, Proc. 12th Cong. IAHR. Fort Collins, Colorado, Vol. 1, 370-378 (1967).
- Callander, R. A., Instability and river channels, J. Fluid Mech., 36, 465-480 (1969).
- Callander, R. A., River meandering, Ann. Rev. Fluid Mech., 10, 129-158 (1978)
- Crow, S.C. and Champagne, F.H., Orderly structure in jet turbulence, Journal of Fluid Mechanics, 48, 547-591 (1971).
- Den Hartog, J.P., Strength of Materials, Dover, New York (1961), Chapter IX.
- Dury, G. H., Principles of underfit streams, U.S. Geol. Survey Prof. Paper 452-A (1964).
- Keller, E. A., Development of alluvial stream channels: a five-stage model, Geol. Soc. America Bull., 83, 1531-1536 (1972).
- Engelund, F. and Skovgaard, O., On the origin of meandering and braiding in alluvial streams, J. Fluid Mech., 57, 289-302 (1973).
- Gorycki, M. A., Hydraulic drag: a meander initiating mechanism, Geol. Soc. America Bull., 84, no. 1, 175-186 (1973a).
- Gorycki, M. A., Hydraulic drag: a meander initiating mechanism: Reply, Geol. Soc. America Bull., 84, no. 9, 3119-3122 (1973b).

- Hansen, E., The formation of meanders as a stability problem, Hydraul. Lab., Tech. Univ. Denmark, Basic Res. Prog. Rep. no. 13 (1967).
- Hayashi, T., The formation of meanders in rivers, Proc. Japan Soc. Civil Engrs., no. 180 (1970).
- Leopold, L. B., and Wolman, M. G., River meanders, Bull. Geological Soc. America, 71, 769-794 (1960).
- Leopold, L. B. and Wolman, M. G., River channel patterns, in Dury G. H., ed., Rivers and River Terraces, Praeger Publishers, New York (1970).
- Leopold, L. B., Wolman, M. G. and Miller, J. P., Fluvial processes in geomorphology, W. H. Freeman, San Francisco (1964).
- Love, A. E. H., The mathematical theory of elasticity, 4th ed., Cambridge University Press, Cambridge (1927), p. 3.
- Parker, G., On the cause and characteristic scales of meandering and braiding in rivers, J. Fluid Mech., 76, 457-480 (1976).
- Prandtl, L., Essentials of Fluid Dynamics, Blackie & Son, London, Chapter II, (1969).
- Schumm, S. A., and Khan, H. R., Experimental study of channel patterns, Geol. Soc. America Bull., 83, 1755-1770 (1972).
- Stommel, H., Circulation in the North Atlantic Ocean, Nature, 173, 886-893 (1954).
- Sukegawa, N., Conditions for the occurrence of river meanders, J. Faculty Eng., Univ. Tokyo, 30, 289-306 (1970).

Tanner, W. F., Helical flow, a possible cause of meandering, J. Geophys. Res., 65, 993-995 (1960).

Tanner, W. F., Inexpensive models for studying helical flow in streams, J. Geol. Education, 10, no. 4, 116-118 (1962).

Turner, J. S., Buoyancy effects in fluids, Cambridge University Press, Cambridge (1972), Figs. 6.2(a), 7.15.

Von Arx, W. S., Notes on the surface velocity profile and horizontal shear across the width of the Gulf Stream, Tellus, 4, 211-214 (1952).

Werner, P. W., On the origin of river meanders, Trans. Am. Geophys. Un. 32, 898-902 (1951).

Reference	λ/W
Werner (1951)	$\sim 2F$
Hansen (1967)	$7F^2 H/(SW)$
Anderson (1967)	$\text{constant} \times (FH/W)^{1/2}$
Hayashi (1974)	$72(FH/W)^{1/2}, F < 1$
Parker (1976)	$2\psi(\pi FH/C_0 W)^{1/2}$

Table 1

Examples of hydrodynamic stability theoretical predictions for the ratio meander wavelength : width

— time, or direction of meander amplitude growth ↓	Reference	λ/W	Remarks
	present theory	2.22	incipient buckling (absolutely straight stream)
	Gorycki (1973a)	2-3	stream plate simulations
	Leopold, Wolman and Miller (1964), Leopold and Wolman(1970) Dury (1964)	2-3	field studies in straight rivers
	Schumm and Khan (1972) Table 3	3.24 ± 0.64	laboratory channel during development
	Keller (1972)	3-5	channel experiments during development
		5-7	during late stages of development
	Leopold and Wolman(1960) Table 1	6.5 - 11	natural (long history)

Table 2

Comparison of the present theory with meander wavelength observations

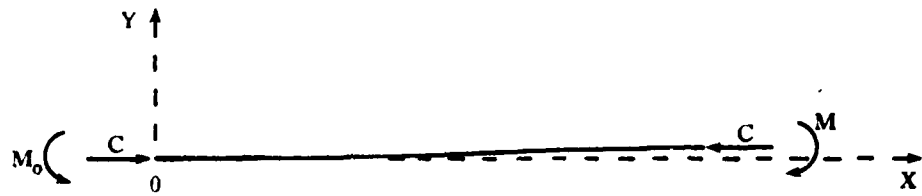


Figure 1. Static equilibrium of a straight river bed (view from above).

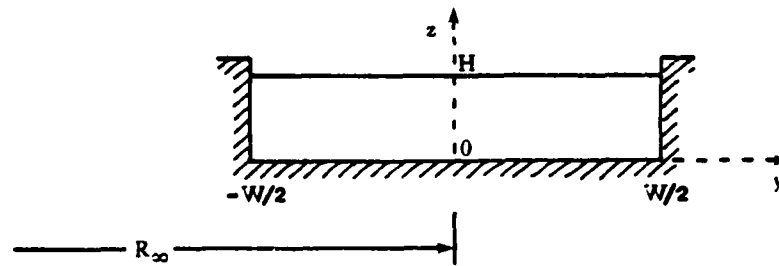


Figure 2. Cross-section through the river.

SECTION 6

Buckling Theory of Momentum and Heat Transfer
in Turbulent Boundary Layer Flow *

by

Adrian Bejan

Department of Mechanical Engineering
University of Colorado
Boulder, Colorado 80309

Abstract

This paper reconstructs theoretically the instantaneous structure of turbulent boundary layer flow. At the very base of this structure rests the newly-discovered buckling property of inviscid fluid layers. The instantaneous structure of the boundary layer reveals the spatial distribution of contact spots (points of direct contact between wall and free stream). The contact spot distribution is used to calculate the skin friction coefficient and the Stanton number. These theoretical predictions agree with experiments, and provide a theoretical explanation for the analogy between fluid friction and heat transfer in turbulent boundary layer flow.

*appears in abbreviated form in: A. Bejan, Entropy Generation through Heat and Fluid Flow, Wiley, New York, 1982, chapter 4.

Nomenclature

A	cross-sectional area of fluid layer
C	impulse, eq. (1)
$C_{f,n}$	skin friction coefficient averaged over n buckling and rolling events, eq. (30)
C_f	average skin friction coefficient, eq. (33)
$C_{f,\delta}$	local skin friction coefficient, eq. (35)
c_p	specific heat at constant pressure
D	thickness of fluid layer
D_o	size of the smallest eddy, eq. (15)
E	modulus of elasticity, eq. (3)
f	natural frequency of shear flow fluctuation, eq. (11)
h_ζ	local heat transfer coefficient, under each contact spot, eq. (36)
h	heat transfer coefficient averaged over the contact spot, eq. (38)
h_n	heat transfer coefficient averaged over n buckling and rolling events, eq. (41)
I	area moment of inertia [2]
k	thermal conductivity
ℓ	length of contact spot, eq. (38)
L_o	laminar tip length of free shear flow, eq. (30)
L_{contact}	sum of wall length covered by contact spots
L_{total}	total wall length
M	bending moment
n	number of buckling and rolling events

N_B	buckling number, eq. (14)
Pr	Prandtl number
R_∞	radius of curvature
Re_δ	Reynolds number based on boundary layer thickness, eq. (32)
Re_θ	Reynolds number based on momentum thickness (Table 2)
St	Strouhal number, only in eq. (12); otherwise Stanton number
St_n	Stanton number averaged over n buckling and rolling events, eq. (42)
St_δ	local Stanton number
t_o	time scale of the first buckling and rolling event, eq. (7)
t_v	time of transversal viscous diffusion, eq. (13)
\bar{T}	period of bursting, eq. (21)
u_*	friction velocity, eq. (26)
U_∞	free stream velocity
V	relative velocity, (Fig. 1)
y_o^+	extent of the dimensionless viscous sublayer, eq. (25)
δ	boundary layer thickness
δ^*	displacement thickness, eq. (39)
δ_{viz}^*	visual growth rate
ϵ	dissipation rate per unit mass
η	Kolmogorov microscale, eq. (16)
θ	momentum thickness
θ_o^*	function of Pr , eq. (37)
λ_B	buckling wavelength
μ	viscosity
ν	kinematic viscosity
ζ	coordinate along the contact spot
ρ	density
τ_o	wall shear

Introduction

The object of this article is to outline a theory which explains the observed features of turbulent shear flow, and also predicts the heat and momentum transfer rates in turbulent boundary layer flow. The theory is based on the recent discovery of the basic property of inviscid fluids which is responsible for turbulent (non-laminar) fluid motion [1]. This property, previously unknown, is the buckling wavelength of inviscid fluid fibers, which, as a property, is analogous to the buckling wavelength (or critical load) of elastic rods in axial compression. It has been demonstrated in Ref. [1] that, like elastic rods, any inviscid layer of fluid satisfies the two conditions necessary for infinitesimal buckling in axial compression:

(i) If the fluid fiber moves at speed V through (relative to) the ambient fluid, then the control surface surrounding the straight fiber is in a state of axial compression. The axial compressive load is the impulse

$$C = \rho V^2 A \quad (1)$$

where ρ is the fluid density and A is the cross-sectional area of the inviscid fluid fiber.

(ii) If the fluid fiber (ρ , A , V) is bent (curved) in a separate bending apparatus, then the fiber cross-section develops a net bending moment oriented in the direction of bending the fiber. In the limit of vanishingly small curvature, $D/R_\infty \rightarrow 0$, the cross-sectional bending moment is proportional to the curvature,

$$M = \rho V^2 I \frac{1}{R_\infty} \quad (2)$$

In this expression, I is the area moment of inertia [2], and R_∞ is the radius of curvature. Equation (2) is analogous to the proportionality between bending moment and curvature encountered in elastic beam theory [3],

$$M = EI \frac{1}{R_\infty} . \quad (3)$$

Therefore, comparing equations (3) and (2), we can regard (ρV^2) as the "elasticity modulus" of the inviscid fluid fiber (for this reason garden hoses become stiffer, i.e. harder to bend, when the flowrate increases).

Conditions (1) and (2) guarantee the existence of a characteristic buckling wavelength [4]. As shown in Ref. [1], the buckling wavelength (λ_B) scales only with the transversal dimension of the fiber (D),

$$\lambda_B = 2\pi \sqrt{\frac{I}{A}} . \quad (4)$$

If the fluid fiber is two-dimensional (thickness D , width W) we have $A = DW$ and $I = D^3W/12$, hence

$$\frac{\lambda_B}{D} = \frac{\pi}{\sqrt{3}} = 1.81 \quad (5)$$

The constancy of the ratio λ_B/D is a property of the fluid fiber. This property exists whether or not the fiber moves relative to its ambient (note that λ_B/D is independent of V). If the fiber does not move relative to its ambient then the static equilibrium of the straight fiber is indifferent and, as a result, the fiber does not buckle. This is the case of fluid layers of all thicknesses in a stationary pool.

If the fiber moves with velocity V relative to its ambient, then the static equilibrium of the straight (infinitesimally buckled) fiber is unstable (see "Rayleigh's Theorem" [5]). In fact, it is the post-buckling evolution of the inviscid fiber which forms the subject of "Hydrodynamic Stability" studies. The buckling property (4) identified in Ref. [1] supplies the part which has been missing from Hydrodynamic Stability studies, namely, the initial condition. It is worth recalling that any stability study begins with postulating the existence of an arbitrary "disturbance"; the buckling property of inviscid fibers explains the origin (source) of the "disturbance" assumed empirically by the stability analyst. In addition, the buckling property states that the "disturbance" is unique, i.e., its wavelength is fixed when the thickness of the fiber is fixed.

The buckling property of inviscid fluid provides for the first time a theoretical basis for predicting the documented features of turbulent fluid behavior. For example, in Ref. [1] the buckling property was shown to be responsible for: 1. the transition to turbulence in free jet (and wake) flow, 2. the natural frequency of turbulent jet flows, and 3. the existence of a Reynolds number considerably greater than unity, as landmark for the transition to turbulent flow. In this paper we focus on the free shear flow and on the boundary layer flow, and demonstrate that the buckling property is responsible for many of the classical characteristics of these flows. We shall rely on the buckling property to reconstruct the instantaneous structure of buckling shear flows: on this basis we can predict theoretically the rates of momentum and heat transfer from a solid wall in turbulent boundary layer flow.

The rolling of buckled shear layers

We begin with the observation that for a two-dimensional fluid layer to become unstable and buckle, its two interfaces with the ambient do not necessarily have to experience relative movement in the same direction (as in the case of a jet or a wake, Ref. [1]). A free shear layer may be modeled as a layer of stationary fluid sandwiched between semi-infinite fluid reservoirs moving in opposite directions. This model is presented in Fig. 1 where a layer of thickness D is swept on both faces by streams of velocity V . Each interface is unstable [6], hence, the amplitude of the buckled layer grows to the point where the crests of the wave get caught in the adjacent streams and roll up.

In a frame of reference which is attached to the shear layer, the layer buckles and rolls up repeatedly. The net result of this sequence of events is that the thickness D grows stepwise in time. A shear layer of initial thickness D_0 will first buckle over a length

$$\lambda_{B,0} = 1.81 D_0 \quad (6)$$

Next, it takes a time of order

$$t_0 \sim \lambda_{B,0}/V \quad (7)$$

for this first wave to roll up into a number of eddies of diameter

$$D_1 \sim 2D_0 \quad (8)$$

As shown in Fig. 2, the new eddies constitute a thicker shear layer of thickness D_1 which buckles immediately over a longer length,

$$\lambda_{B,1} = 1.81 D_1 \quad (9)$$

The buckling and rolling up process repeats itself, producing as observable result a conglomerate of eddies, small eddies rolled up inside larger eddies (hence, the phenomenon of "vortex pairing"). In time, the birth of the small eddy preceeds the birth of the next size, larger, eddy.

In another frame of reference which is stationary with respect to one of the uniform streams, the shear layer flares out linearly in the direction of the moving stream ($U_\infty = 2V$). The structure of the shear layer is shown schematically in Fig. 3. Each eddy travels a distance λ_B during one roll up time interval $t \sim \lambda_B/V$; during the same time interval, the thickness of the shear layer grows by a factor of order 2, eq. (7). Therefore, the visual growth rate δ'_{viz} defined by Brown and Roshko [7] is a constant,

$$\delta'_{viz} \sim \frac{D}{\frac{3}{2} \lambda_B} \sim 0.37, \text{ constant} \quad (10)$$

This order-of-magnitude estimate agrees very well with experimental observations [7].

The repeated buckling of the shear layer provides an explanation for the observed phenomenon of "resonance" in shear layers subjected to external forcing. Freymuth [8] showed experimentally that the response of the shear layer is such that the diameter of the most regular roll increases as the

as the frequency of external excitation decreases. At the same time, the longitudinal location of the most regular roll moves downstream.

Relative to the observer at rest in one of the semi-infinite fluids, the shear layer fluctuates (waves) with a frequency

$$f = \frac{v}{\lambda_B} = 0.276 \frac{U_\infty}{D} \quad (11)$$

Therefore, the Strouhal number based on U_∞ and local shear layer thickness D is a universal constant

$$St = \frac{f D}{U_\infty} = 0.276. \quad (12)$$

Now, we are entitled to expect the natural frequency of the shear layer to decrease in the downstream direction because the thickness D increases linearly. Measurements reported recently by Hussain and Thompson [9] confirm the theoretical conclusion that the size and axial location of the resonating roll must vary inversely with the frequency of external excitation, eq. (11).

In this section we reviewed a series of classical observations, all of which support the view that the turbulence and growth of free shear layers is due to the repeated buckling and rolling phenomenon illustrated in Fig. 2. Unfortunately, the "rolling" part of the phenomenon wipes out the "buckling" part which serves as origin for the entire process. There are special cases in which the amplitude of the buckled layer cannot grow to approximately $D/2$, as in Fig. 2; consequently, the "rolling" phase is avoided, and the wavy shape of the buckled layer is visible to the eye. Such is the case of shear

layers in stably stratified fluids. Thus, attention is drawn to Fig. 8 published in Thorpe's study of the instability of stably stratified shear flows [10]: the wavelength of the buckled shear layers is of order 3 cm which, compared with the layer thickness $D = 1.5$ cm, proves the existence of the natural buckled shape shown in Fig. 1.

Transition to turbulence in shear flow: the smallest eddy

Consider the shear flow sketch in Fig. 4, where the initial velocity profile (a) shows a shear layer of zero thickness. It is well established that if the fluid is modeled as inviscid throughout, the (a) profile is unstable [5]. However, it is wrong to regard the zero-thickness shear region of the (a) profile as inviscid, because the viscous communication time across this region is infinitely short (see the definition of the Buckling Number, Ref [1]). Therefore, in the very beginning of the shearing phenomenon, the growth of the shear zone is governed by the viscous transfer of momentum. Laminar, Couette-type, flow prevails until the layer is thick enough so that the viscous communication time across the layer exceeds the duration of the first buckling and rolling event. Only beyond this point is the layer able to behave inviscidly and roll up.

The viscous communication time t_v from the interface to the middle of the layer (distance $D/2$) can be evaluated from Stokes' first problem [11],

$$\frac{D/2}{2\sqrt{\nu t_v}} \sim 1, \text{ hence } t_v \sim \frac{D^2}{16\nu} \quad (13)$$

The time of the first buckling and rolling event is given by eq. (6), where $V = U_\infty/2$. At transition, the Buckling Number is of order one,

$$N_B = \frac{t_v}{t_0} \sim 1 \quad (14)$$

hence

$$\frac{U_\infty D_0}{\nu} \sim 58 \quad (14')$$

A first consequence of this result is that the turbulent shear layer will contain rolls with diameters larger than

$$D_o \sim 58 \frac{\nu}{U_\infty} \quad (15)$$

This conclusion is verified qualitatively by the size of the "loops" visible in the shadowgraph networks reported by Brown and Roshko [7]. According to eq. (15), the "fineness" of the ensuing turbulent flow is enhanced (the loops get smaller) when the original velocity discontinuity U_∞ increases.

Interestingly enough, the size of the smallest eddy, eq. (15), is a refined statement of the Kolmogorov microscale [12],

$$\eta = \left(\frac{\nu^3}{\epsilon} \right)^{1/4} \quad (16)$$

where ϵ is the local dissipation rate per unit mass. In the present discussion, the local dissipation rate in profile (b) (Fig. 4), just before the first buckling and the first roll, is

$$\epsilon \sim \nu \left(\frac{U_\infty}{D_o} \right)^2 \quad (17)$$

Substituting this estimate into the Kolmogorov microscale (16) we obtain

$$\eta \sim \frac{D_o}{\sqrt{58}} = \frac{D_o}{7.6} \quad (18)$$

We conclude that, although η is proportional to D_o , the eddy of size η

s too small to be able to exist: this is due to the fact that the Reynolds number based on the Kolmogorov length scale is of order one [12] and the Buckling Number is considerably smaller than one [1]. As shown in Ref. [1] and in the remainder of this paper, classical observations of turbulence support the theoretical conclusion (14, 14') that turbulent flow is possible only above a Buckling Number of order one (i.e., above a Reynolds number considerably greater than one).

Another consequence of the transition criterion (14) is that the leading section of the shear layer, region (a) - (b) on Fig. 4, remains laminar over a characteristic length L_o . This length is equal to the distance traveled by the free stream U_∞ during a time interval equal to the critical viscous diffusion time $t_v (= t_o)$,

$$L_o \sim U_\infty t_v. \quad (19)$$

Combining equations (19), (14') and (13) we obtain

$$\frac{U_\infty L_o}{\nu} \sim 210 \quad (20)$$

Therefore, the laminar length decreases when the velocity discontinuity U_∞ increases. This conclusion is in agreement with the sequence of photographs reported as Fig. 20 in Ref. [7]. We make the final observation that the laminar tip length L_o and the smallest eddy diameter D_o are proportional,

$$\frac{L_o}{D_o} \sim 3.64. \quad (20')$$

In other words, regardless of Reynolds number^{*}, the shapes of all shear flow regions are geometrically similar: the geometric similarity rules both regions, the laminar tip region (Fig. 4) and the buckling and rolling wedge region (Fig. 3).

The periodic bursting of boundary layers

We now turn our attention to the instantaneous structure of turbulent wall layers. Over the past two decades, considerable experimental work on wall turbulence has shown that this process is composed of a sequence of events having a definable overall period \bar{T} [13]. In one phase of the process, free-stream fluid rushes in close to the wall, and in the next phase the laminar sublayer "bursts" and gives birth to large scale eddies. It was found that the period of this "bursting" process scales with the outer flow parameters (U_∞, δ),

$$\frac{U_\infty \bar{T}}{\delta} \sim 5, \quad (21)$$

where δ is the boundary layer thickness and U_∞ the free-stream velocity. As commented by Laufer and Narayanan [14], it may seem intriguing that a process which "occurs in the viscous sublayer" should scale with the outer flow parameters. As shown next, the explanation lies in the fact that the bursting process does not occur in the viscous sublayer, but in the outer layer (the viscous sublayer is merely the time-averaged footprint of the bursting process).

The buckling of shear layers accounts for the periodicity of the "bursts" phenomenon. The instantaneous structure of a wall layer can be reconstructed geometrically, step-by-step, in the same manner as the structure of a free shear layer (Figs. 3,4). The geometric construction is shown in Fig. 5. Close to the leading edge of the solid wall, the buckling and rolling sequence generates a shear layer which is similar to what we have seen already in Figs. 3 and 4. Further downstream, however, each subsequent roll triggers a new shear layer

^{*} based on a fixed laboratory length, such as nozzle diameter [9]

nestled inside the original one. We shall return to this instantaneous structure in the next section where we estimate the wall friction characteristics.

To predict the bursting period \bar{T} , we make the observation that at a fixed location x along the wall, the original (thickest) shear layer buckles over a length

$$\lambda_B \sim 1.81 \delta, \quad (22)$$

where δ is the physical extremity of the boundary layer. From symmetry, the local buckled wave (22) travels to the right at a speed of order $U_\infty/2$. Therefore, the free stream U_∞ makes contact with a fixed spot on the wall periodically, at intervals of order

$$\bar{T} \sim \frac{\lambda_B}{U_\infty/2} \quad (23)$$

In other words, when

$$\frac{U_\infty \bar{T}}{\delta} \sim 3.8. \quad (24)$$

This theoretical, order-of-magnitude, result is in very good agreement with the growing body of experimental data on the period of bursting [15].

It is easy to show that the thickest stable laminar layer, D_0 , eq. (15), represents the thickness of what is experimentally identified as "viscous sublayer". The dimensionless wall coordinate corresponding to D_0 is

$$y_o^+ = \frac{D_o u_*}{\nu} \quad (25)$$

where the friction velocity* is of order

$$u_* = \sqrt{\tau_o / \rho} \sim \sqrt{\nu U_\infty / D_o} \quad (26)$$

Combining expressions (25) and (26), we predict

$$y_o^+ \sim \sqrt{D_o U_\infty / \nu} = \sqrt{58} = 7.62 \quad (27)$$

which is, of course, the extent of the laminar sublayer in the measured universal velocity profile.

We conclude that the "viscous sublayer" is another manifestation of the stable laminar length which precedes the first buckling event in the development of any shear layer (Fig. 4). The viscous sublayer is also a manifestation of the smallest eddy size determined in the preceding section, eq. (15).

* instantaneous (not time-averaged) estimate, on the spot where the free stream "hits" the wall

The skin friction coefficient

The instantaneous boundary layer structure constructed in Fig. 5 is a tool for predicting the rate of momentum transfer from the stream to the wall. Figure 5 was constructed based on the following shear flow properties (identified in the earlier sections of this paper):

- a) the shear layer of thickness δ buckles and rolls over a precise length, 1.81δ , eq. (8).
- b) the "in rush" phase of the "roll" process brings free stream fluid in contact with the wall: a secondary shear layer is triggered anytime this contact is made.
- c) the "burst" phase of the "roll" process takes stationary fluid out into the free stream: when this happens, the secondary shear layer is terminated.

The resulting structure of the boundary layer has a characteristic stepwise, linear growth: the primary and secondary shear layers are bounded from above by a "characteristic upstream interface" [15]. The angle between the upstream interface (dashed line on Fig. 5) and the solid wall is a universal constant for all turbulent boundary layers,

$$\arctan \left[\frac{D}{\frac{3}{2} \lambda_B} \right] = \arctan (0.368) = 20.18^\circ \quad (28)$$

It is worth noting that this angle is precisely the one photographed and measured recently by Bandyopadhyay [15]. Note further that Bandyopadhyay's photographs, especially Figs. 1(c), (d), show wall structures which grow stepwise in the downstream direction, as in Fig. 5.

The calculation of the instantaneous wall shear stress distribution consists of summing-up the wall length covered by laminar shear zones (these zones are shown cross-hatched on Fig. 5). As demonstrated in the preceeding section, the thickness of the laminar shear zone (the viscous sublayer) is fixed as soon as U_∞ is specified (eq. 27). However, the free stream does not make contact with the wall over its entire length; the contact is discrete and less frequent as the boundary layer thickness increases. This wall friction mechanism differs fundamentally from the mechanism known in laminar flow and, indeed, from the laminar-like mechanism suggested by the concept of time-averaged (universal) velocity profile in turbulent flow. The laminar mechanism is one where the velocity gradient evaluated at the wall decreases continuously in the downstream direction. In Fig. 5, the velocity gradient is always of order U_∞/D_0 , regardless of x , but only in those special spots where the free steam "rushes" into the wall. The real contribution of the buckling theory employed in this paper is that it identifies the spatial sequence of the "inrush" events.

There are a number of ways in which one could extract skin friction information from Fig. 5. Since, as engineers, we are primarily interested in the friction effect averaged over the length of the wall, we will first sum up the contact length, L_{contact} , over a specified wall length, L_{total} . In view of the stepwise-growing structure of the primary layer, it makes sense to focus on a discrete sequence of wall lengths: each length (L_{total}) corresponds to an integral number of buckling and rolling events (n). The results of this calculation are reported in Table 1 (note that the structure of Fig. 5 is drawn to scale, where the length unit in both directions is D_0). The table extends well beyond the $n = 4$ wall

length illustrated in Fig. 5: this extension is made possible by the observation that successive values of $L_{\text{contact}}/L_{\text{total}}$ are related through the following recurrence relationship:

$$\left(\frac{L_{\text{contact}}}{L_{\text{total}}} \right)_n = \frac{L_{\text{contact},n-1} + L_{\text{contact},n-2}}{2 L_{\text{total},n-1}} \quad (29)$$

The average skin friction coefficient for the wall length $L_{\text{total},n}$ is

$$C_{f,n} = \frac{\tau_{\text{avg}}}{\frac{1}{2} \rho U_{\infty}^2} = \frac{\mu U_{\infty}/D_o}{\frac{1}{2} \rho U_{\infty}^2} \left(\frac{L_{\text{contact}}}{L_{\text{total}}} \right)_n \quad (30)$$

which, using the smallest eddy criterion (15), becomes

$$C_{f,n} \sim \frac{2}{58} \left(\frac{L_{\text{contact}}}{L_{\text{total}}} \right)_n \quad (31)$$

The numerical values of $C_{f,n}$ are listed also in Table 1. The corresponding Reynolds number, based on the end-thickness of the primary boundary layer (δ), is

$$Re_{\delta} = \frac{U_{\infty} \delta}{\nu} = \left(\frac{\delta}{L_{\text{total}}} \right)_n \frac{D_o U_{\infty}}{\nu} \frac{L_{\text{total},n}}{D_o} \quad (32)$$

This number is readily calculated, noting again that $D_o U_\infty / \nu \approx 58$ and $(\delta/L_{total})_n \approx 0.37$.

Figure 6 shows the relationship between the length-averaged skin friction coefficient, C_f , and the Reynolds number corresponding to the end thickness, Re_δ . Owing to the recurrence relation (29), the points line up according to a power law,

$$C_f = 0.122 Re_\delta^{-0.304} . \quad (33)$$

Finally, we can use eq. (33) to deduce the local skin friction coefficient $C_{f,\delta}$, defined via

$$C_f = \frac{1}{\delta} \int_0^\delta C_{f,\delta} d\delta . \quad (34)$$

We obtain

$$C_{f,\delta} = 0.0849 Re_\delta^{-0.304} \quad (35)$$

Expression (35) is shown plotted on Fig. 6 next to experimental data obtained at low Reynolds numbers [16]. Before discussing the agreement between the present theory and the experimental evidence, it is important to note that the experimental results are not available in the $C_{f,\delta} - Re_\delta$ language employed in Fig. 6. In Ref. [16], for example, the boundary layer thickness δ is not reported at all: instead, the experimental measurements are catalogued in terms of the momentum thickness

0 and the Reynolds number based on the momentum thickness Re_θ . The author of the present paper was able to calculate δ (hence Re_δ) from the actual, time-averaged, velocity profiles measured but not reported by Purtell et al [16] (the author received copies of these measurements privately [17]). The boundary layer thickness δ was calculated by extrapolating linearly beyond the last three (outer) points of the time-averaged velocity profile (all these points fall in the range $0.95 < \bar{u}/U_\infty < 1.00$). This calculation procedure is justified, because, unlike in laminar boundary layer flow where the definition of δ is based on convention, in turbulent flow the instantaneous frontier between wall fluid and free stream is always a distinct, sharply defined, line (see Bandyopadhyay's photographs [15], and the concept of "intermittency" [18, 19]). The resulting Re_δ corresponding to the eleven experiments described by Purtell et al [16] is reported here in Table 2.

Turning our attention back to Fig. 6, we find good agreement between equation (35) and experiment. Although encouraging, the small (20%) discrepancy between the theoretical and experimental values of $C_{f,\delta}$ is not the true measure of the "good" agreement (this is due to the fact that, numerically, expression (35) represents only an order-of-magnitude estimate). The important measure of the agreement is in the slope of the $C_{f,\delta} - Re_\delta$ line (note that in constructing Fig. 5 and eq. (35) we applied consistently the universal geometric properties of buckling shear flows, as discussed in the beginning of this section). The reliance on this universal structure of buckling shear flow is responsible for Fig. 5 and, via the recurrence formula (29), for the -0.304 exponent in the $C_{f,\delta}$ expression (35). The theoretical line (35) is parallel to the experimental data in the range $Re_\delta \leq 17140$; this suggests that the two-dimensional boundary layer model envisioned in this paper becomes less adequate as the wall layer grows beyond the 7th or 8th buckling and rolling event.

The heat transfer coefficient

The heat transfer rate in turbulent boundary layer flow can be calculated by reading Fig. 5, i.e., by counting the actual spots of direct thermal contact between wall and free stream. Under each contact spot, the local heat transfer coefficient is given by Pohlhausen's solution [20]

$$h_{\zeta} \approx k \theta'_0 \left(\frac{U_{\infty}}{\nu \zeta} \right)^{1/2} \quad (36)$$

where θ'_0 is a Pr - function which, for fluids other than liquid metals, is approximated by [21]

$$\theta'_0 \approx 0.332 \text{ Pr}^{1/3}, \quad \text{Pr} > 0.5 \quad (37)$$

Averaging the local heat transfer coefficient (36) over the entire length of the contact spot, $0 < \zeta < \ell$, we obtain

$$h = 2 k \theta'_0 \left(\frac{U_{\infty}}{\nu \ell} \right)^{1/2} \quad (38)$$

We note also that at $\zeta = \ell$ the displacement thickness of the laminar contact spot is [22]

$$\delta^* = \frac{5}{3} \left(\frac{\nu_{\infty}}{\nu \ell} \right)^{-1/2} \quad (39)$$

In view of the simple (uniform flow) shear layer model employed in the present theory (Fig. 1), we identify δ^* as equal to D_0 ; combining this result with equations (38) and (15) we obtain

$$h \approx \frac{5}{87} k \theta_o' \frac{U_\infty}{\nu} \quad (40)$$

As in the calculation of skin friction coefficient, eq. (30), the heat transfer coefficient averaged over n buckling and rolling events is

$$h_n \approx \frac{5}{87} k \theta_o' \frac{U_\infty}{\nu} \left(\frac{L_{\text{contact}}}{L_{\text{total}}} \right)_n \quad (41)$$

The ratio $(L_{\text{contact}}/L_{\text{total}})_n$ follows from equations (31) and (33): substituting this ratio into equation (41) we obtain the average Stanton number

$$St_n \approx \frac{h_n}{\rho c_p U_\infty} \approx 0.203 \frac{\theta_o'}{\text{Pr}} \text{Re}_\delta^{-0.304} \quad (42)$$

Finally, based on a definition of type (34), we conclude that the local Stanton number is

$$St_\delta \approx 0.142 \frac{\theta_o'}{\text{Pr}} \text{Re}_\delta^{-0.304} \quad (43)$$

In the range $\text{Pr} > 0.5$, expression (43) reduces to

$$St_\delta \text{Pr}^{2/3} \approx 0.047 \text{Re}_\delta^{-0.304} \quad (44)$$

Equation (44) represents the heat transfer coefficient predicted by the theory constructed in this paper. To test this result, we divide equations (44) and (35) side-by-side, and write

$$\frac{St_{\delta} Pr^{2/3}}{\frac{1}{2} C_{f,\delta}} = 1.11 \quad (45)$$

We find that the theoretical result (44) satisfies the Colburn analogy between turbulent heat transfer and fluid friction [23]. Considering the wealth of experimental evidence supporting the Colburn analogy, and recalling the good agreement between theoretical and experimental skin friction coefficient (Fig. 6), we draw the conclusion that the theoretical result (44) is correct.

An equally important conclusion follows from expression (43), which states that in turbulent boundary layer flow the St - Pr relationship is governed by the proportionality

$$St \sim \frac{\theta_o'}{Pr} \quad (43)$$

It is important to note that this is the same St - Pr relationship encountered in laminar flow. In other words, the present theory states that the Stanton number for laminar and turbulent flow must have the same Prandtl number dependence: this prediction is confirmed by experimental correlations for turbulent heat transfer [24].

Conclusions

This paper outlined a theory which explains the instantaneous structure of turbulent shear flow and boundary layer flow. The theory is built around the newly-discovered buckling property of inviscid fluid layers [1]. Starting from this new property of inviscid flow, we were able to reconstruct many classical examples of "turbulent" behavior in shear flow. Reviewing these examples in order, this paper explained theoretically the origin of:

- a) the phenomenon of vortex pairing (Fig. 2)
- b) the linear growth of free shear layers (Fig. 3 and eq. 10)
- c) The phenomenon of resonance in shear layers subjected to external forcing (eq. 12)
- d) the transition to turbulence in free shear flow (eq. 14)
- e) the size of the smallest eddy (eq. 15)
- f) the stable laminar length at the tip of a shear layer (eq. 20)
- g) the geometrically similar shape of all shear flows (Fig. 4)
- h) the periodic bursting of boundary layers (eq. 24)
- i) the viscous sublayer in turbulent boundary layers (eq. 27)
- j) the 20° slope of the upstream interface in turbulent boundary layers (eq. 28)

Relying on these features and on the buckling length and time scales, λ_B and t_0 , we were able to reconstruct on paper the instantaneous structure of a turbulent boundary layer (Fig. 5). This structure allowed us to calculate the spatial density of the footprints (direct contact spots) made by the free stream on the wall. Using the footprint density, we were able to predict the skin friction and heat transfer coefficients. These predictions are in agreement with experimental results.

The instantaneous boundary layer structure envisioned in the present theory explains also the origin of "an analogy between heat and momentum transfer", in the correlation of turbulent heat transfer and fluid friction measurements (eq. 45). The "analogy" stems from the fact that the density of contact spots is the same for both skin friction and heat transfer; consequently, the skin friction coefficient and the Stanton number exhibit the same dependence on the Reynolds number (see equations 35 and 43).

Overall, this paper advances a new theory of boundary layer flow and heat transfer. It should be recognized that this new theory departs drastically from accepted methodology, because it focuses on the instantaneous structure of turbulent flow rather than on the time-averaged flow. Indeed, it is the focus on the instantaneous structure which is responsible for the success of this new theory: once the instantaneous fabric of the flow is discovered, it is not difficult to evaluate the average quantities one might measure in an actual experiment.

Acknowledgement. This research was conducted under the auspices of the Office of Naval Research (contract no. N00014-79-C-0006).

References

1. A. Bejan, On the buckling property of inviscid jets and the origin of turbulence, Letters in Heat and Mass Transfer, 8, 187-194 (1981).
2. J. P. Den Hartog, Strength of Materials, McGraw-Hill, New York (1949), p. 316.
3. J. P. Den Hartog, Op. Cit., p. 80.
4. J. P. Den Hartog, Op. Cit., p. 184.
5. C. S. Yih, Fluid Mechanics, McGraw-Hill, New York (1969), p. 470.
6. L. Prandtl, Essentials of Fluid Dynamics, Blackie and Son, London (1969), p. 51.
7. G. L. Brown and A. Roshko, On density effects and large scale structures in turbulent mixing layers, Journal of Fluid Mechanics, 64, 775 (1974).
8. P. Freymuth, On transition in a separated laminar boundary layer, Journal of Fluid Mechanics, 25, 683 (1966).
9. A. K. M. F. Hussain and C. A. Thompson, Controlled symmetric perturbation of the plane jet: an experimental study in the initial region, Journal of Fluid Mechanics, 100, 397 (1980).
10. S. A. Thorpe, Experiments on the instability of stratified shear flows: immiscible fluids, Journal of Fluid Mechanics, 39, 25-48 (1969).

11. H. Schlichting, Boundary Layer Theory, 4th edition, McGraw-Hill, New York (1960), p. 72.
12. H. Tennekes and J. L. Lumley, A First Course in Turbulence, The MIT Press, Cambridge, Massachusetts (1972), p. 20.
13. H. T. Kim, S. J. Kline and W. C. Reynolds, The production of turbulence near a smooth wall in turbulent boundary layer, Journal of Fluid Mechanics, 50, 133 (1971).
14. J. Laufer and M. A. B. Narayanan, Mean period of the turbulent production mechanism in a boundary layer, Physics of Fluids, 14, 182, (1971).
15. P. Bandyopadhyay, Large structure with a characteristic upstream interface in turbulent boundary layers, Physics of Fluids, 23, 2326 (1980).
16. L. P. Purtell, P. S. Klebanoff and F. T. Buckley, Turbulent boundary layer at low Reynolds number, Physics of Fluids, 24, 802 (1981).
17. P. S. Klebanoff, Private communication, June 15, 1981.
18. G. B. Schubauer, Turbulent processes as observed in boundary layer and pipe, Journal of Applied Physics, 25, 188 (1954).
19. C. S. Yih, Op. Cit., p.545.
20. E. Pohlhausen, Z. A. M. M., 1, 115 (1921).
21. W. M. Rohsenow and H. Y. Choi, Heat, Mass and Momentum Transfer, Prentice-Hall, Englewood Cliffs, New Jersey (1961), P.147.
22. W. M. Rohsenow and H. Y. Choi, Op. Cit., p.39.
23. W. M. Rohsenow and H. Y. Choi, Op. Cit., p.198.
24. V. S. Arpaci, Observation made during a May 29, 1981, lecture given at the National Center for Atmospheric Research, Boulder, Colorado.

Table 1

n	$L_{\text{contact}}/L_{\text{total}}$	$C_{f,n}$	Re_{δ}
1	$\frac{5.45}{7.26} = 0.751$	0.0259	155
2	$\frac{9.07}{14.5} = 0.626$	0.0216	310
3	$\frac{14.52}{29.06} = 0.50$	0.0172	621
4	$\frac{23.6}{58.1} = 0.406$	0.0140	1241
5	$\frac{38.12}{116.2} = 0.328$	0.0113	2482
6	$\frac{61.72}{232.4} = 0.266$	0.00917	4965
7	$\frac{99.84}{464.8} = 0.215$	0.00741	9930
8	$\frac{161.56}{929.6} = 0.174$	0.00600	19860
9	$\frac{261.4}{1859.} = 0.141$	0.00486	39720

Table 2

R_0	R_δ	C_f
465	4020	0.00544
498	4230	0.00540
700	6560	0.00483
1000	9230	0.00442
1340	11590	0.00394
1370	12340	0.00402
1840	17140	0.00363
2840	31770	0.00336
3480	32500	0.00320
4090	37240	0.00316
5100	50460	0.00304

List of Captions

- Fig. 1 Incipient buckling of a two-dimensional shear layer.
- Fig. 2 Successive buckling events, as origin of shear layer growth (vortex pairing).
- Fig. 3 Linear growth of a buckling and rolling shear layer.
- Fig. 4 Laminar region at the tip of a two-dimensional shear layer
- Fig. 5 Universal geometric structure of a two-dimensional boundary layer (the structure is drawn to scale, $D_0 =$ length unit).
- Fig. 6 Local skin friction coefficient predicted by the present theory, vis-a-vis experimental data (Table 2).

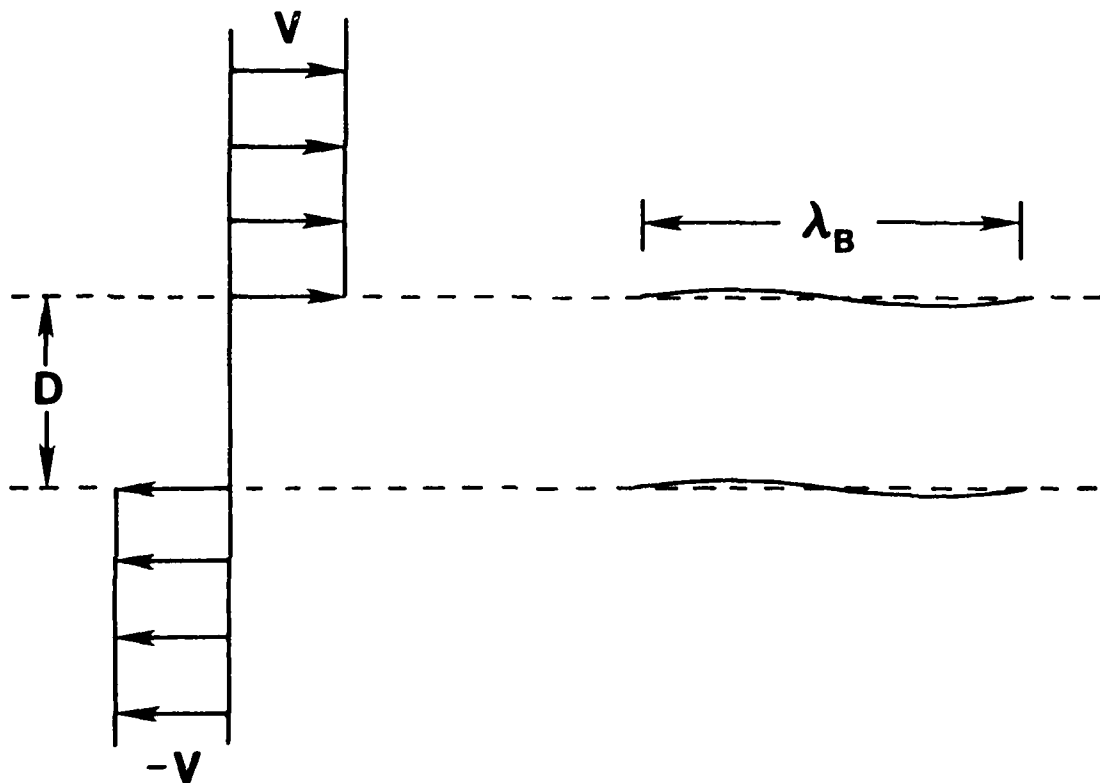
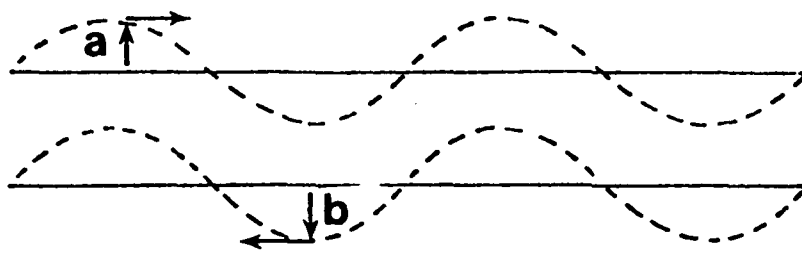
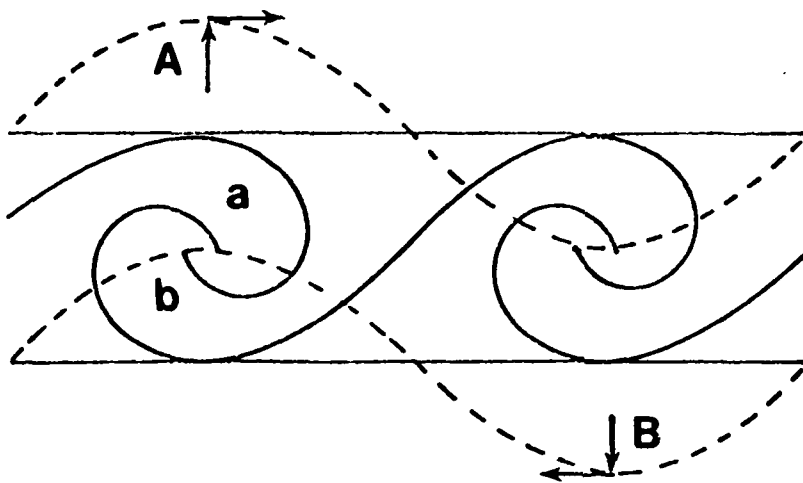


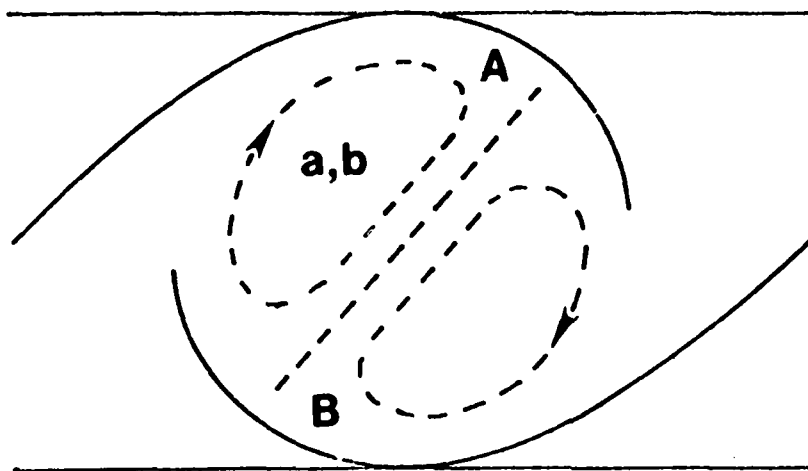
Figure 1



1st buckling



2nd buckling



vortex pairing

Figure 2

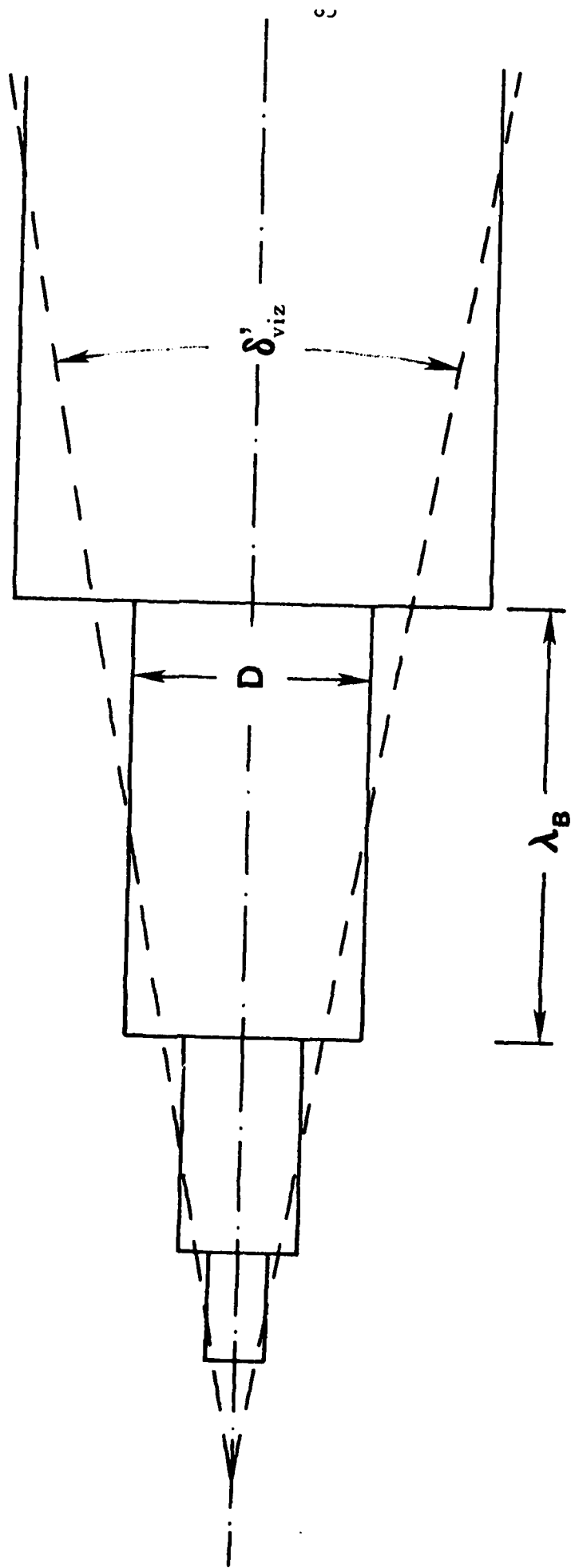


Figure 3

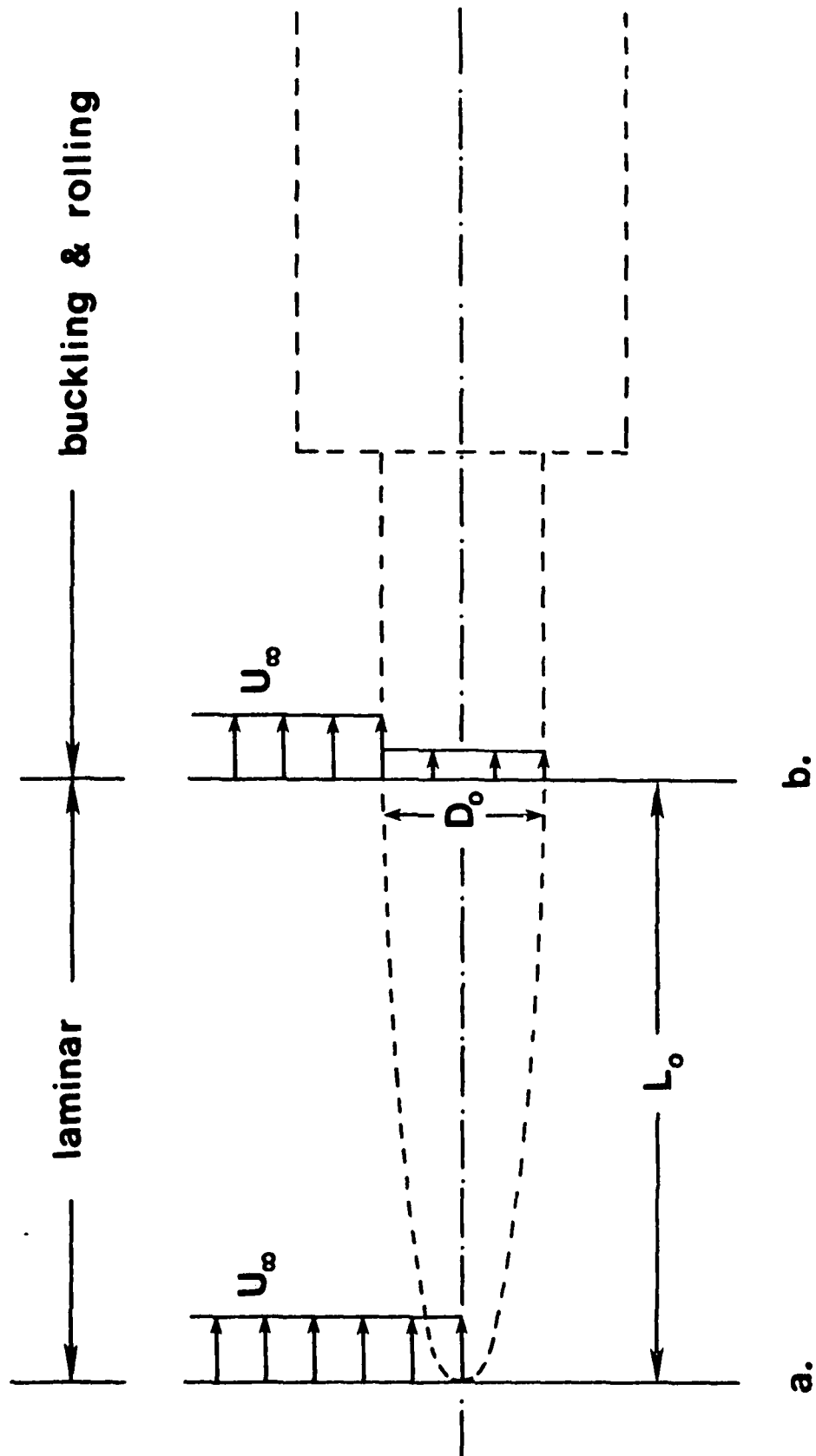


Figure 4

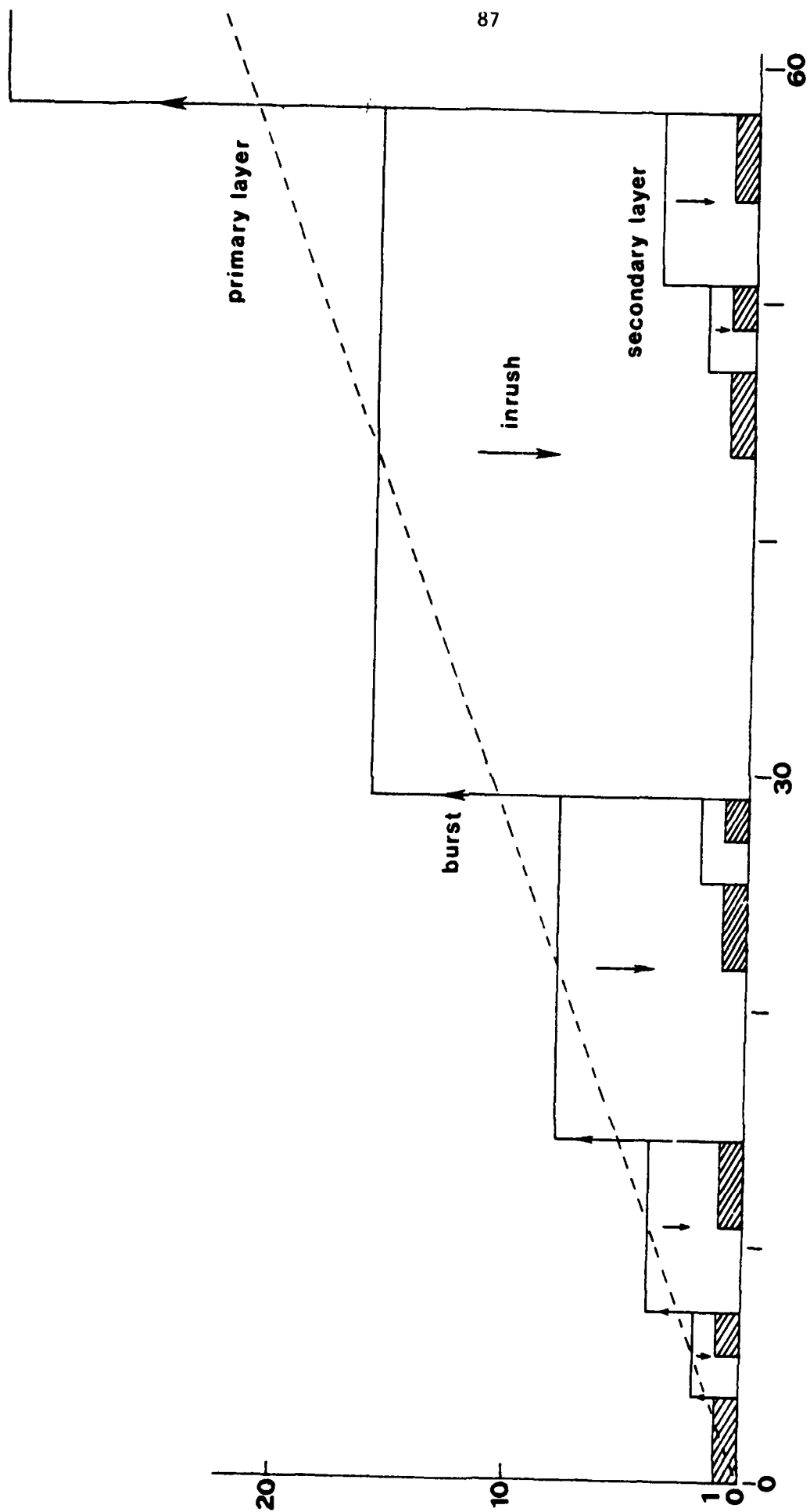


Figure 5

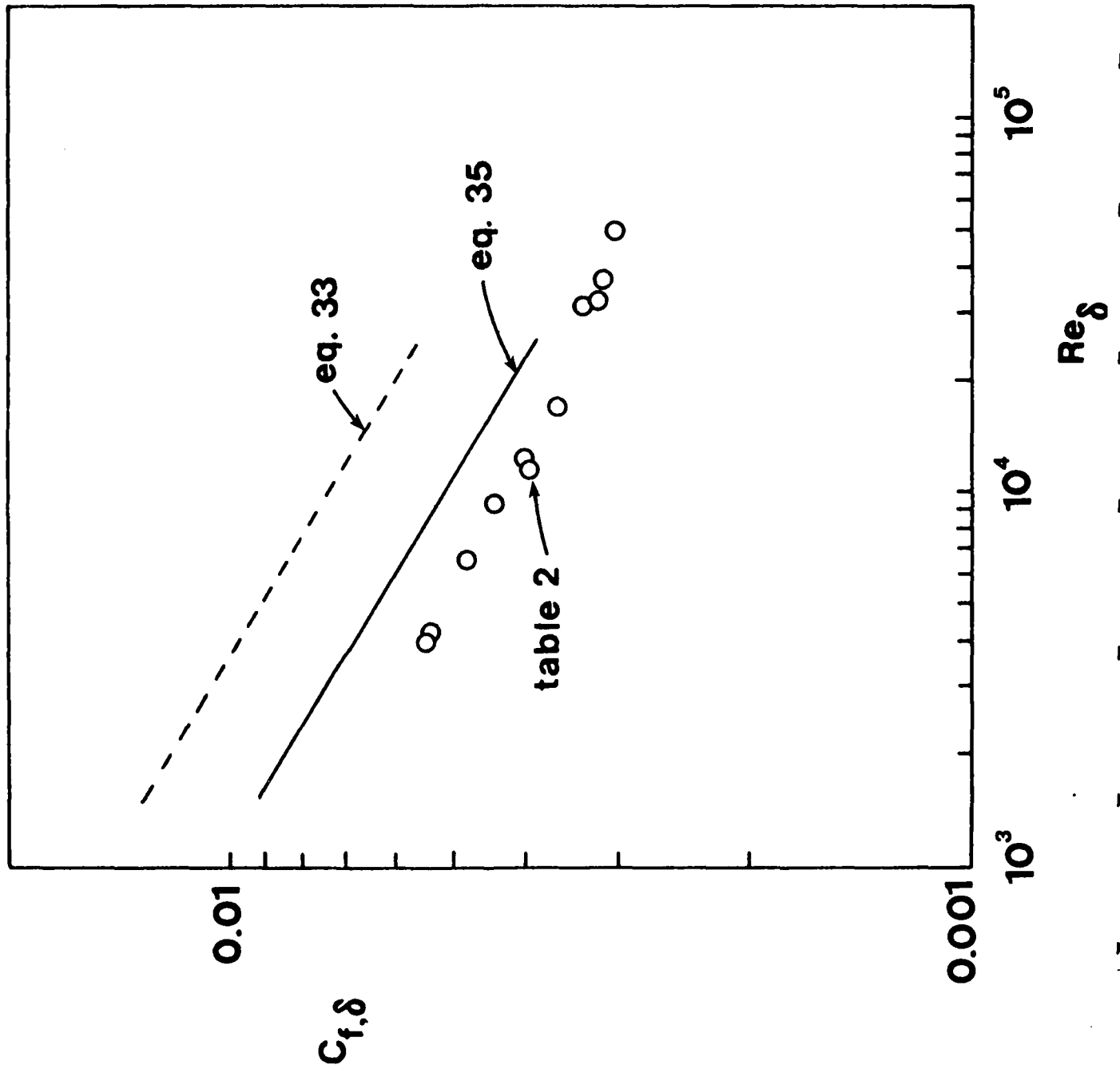


Figure 6

SECTION 7

COMPACT EXPRESSION FOR THE LOCAL DISSIPATION
RATE IN TURBULENT PIPE FLOW^{*}

by

Adrian Bejan
Department of Mechanical Engineering
University of Colorado
Boulder, Colorado 80309

Abstract

This note shows that the local dissipation rate in turbulent pipe flow can be expressed as the mean velocity gradient squared times the sum of molecular and eddy viscosities. This compact expression is suggested by the symmetry between the momentum equation for laminar flow and the time-averaged momentum equation for turbulent flow. It is shown that the integral of this compact expression over the pipe cross-section agrees within 0.5% with overall pumping power loss measurements in a wide Reynolds number range.

* appears in abbreviated form in: A. Bejan, Entropy Generation through Heat and Fluid Flow, Wiley, New York, 1982, chapter 3.

Introduction

Dissipation is one of the central topics in turbulent heat transfer research today. The prominence of this topic is due to a large extent to the wide interest in computational modeling of turbulent flows. The dissipation mechanism is also becoming an important topic in the energy-applications of heat transfer engineering: in such applications, the dissipation mechanism is seen as responsible for the one-way destruction of exergy (available work) in engineering components [1].

The objective of this short technical note is to report a compact expression for the local rate of viscous dissipation in turbulent pipe flow, ϵ . As summarized by Hinze [2], the current approach to determining ϵ consists of the direct measurement of local velocity gradients (see, for example, Laufer's experiments [3]). In view of the generally accepted need for special experiments to measure ϵ directly, it would be advantageous if one could calculate ϵ based on readily available (universal) measurements, rather than on special measurement of the type pioneered by Laufer [3]. The following analysis recommends a simple formula for calculating the local dissipation rate ϵ using the universal velocity profile.

Analysis

The compact expression for ϵ is suggested by the well-known symmetry which exists between the longitudinal momentum equation in laminar pipe flow,

$$0 = -\frac{1}{\rho} \frac{dP}{dx} + \frac{\nu}{r} \frac{d}{dr} \left(r \frac{du}{dr} \right) \quad (1)$$

and the corresponding equation for turbulent flow

$$0 = -\frac{1}{\rho} \frac{d\bar{P}}{dx} + \frac{1}{r} \frac{d}{dr} \left[(\nu + \epsilon_M) r \frac{d\bar{u}}{dr} \right] \quad (2)$$

These equations are written in the usual notation, where ϵ_M is the eddy diffusivity for momentum. The remaining symbols are defined in the Nomenclature.

We now make the important observation that, according to variational calculus [4], the momentum equation for laminar flow (1) is the Euler equation associated with minimizing the integral

$$I_{\text{laminar}} = 2\pi \int_0^r \left[\mu \left(\frac{du}{dr} \right)^2 + 2u \frac{dP}{dx} \right] r dr \quad (3)$$

subject to fixed dP/dx . Likewise, equation (2) follows from minimizing another integral,

$$I_{\text{turbulent}} = 2\pi \int_0^r \left[\rho(\nu + \epsilon_M) \left(\frac{d\bar{u}}{dr} \right)^2 + 2\bar{u} \frac{d\bar{P}}{dx} \right] r dr \quad (4)$$

where $d\bar{P}/dx$ is also imposed. Next, we note that the first term in the integrand of I_{laminar} is exactly the local dissipation rate in laminar flow [1]. Comparing the integrand of $I_{\text{turbulent}}$ with the integrand of I_{laminar} , we must suspect that the expression

$$\epsilon_{\text{model}} = (\nu + \epsilon_M) \left(\frac{d\bar{u}}{dr} \right)^2 \quad (5)$$

occupies the place of the dissipation rate ϵ in turbulent flow.

We can determine the accuracy of model (5) by comparing its predictions with experimental evidence. First, expression (5) is known to be exact

in the viscous sublayer because, in that region, $\nu \gg \epsilon_M$. Second, the accuracy of model (5) can be tested in an integral manner, by integrating the local dissipation rate (5) over the pipe cross-section and comparing the result with overall measurements based on pressure drop data. The pumping power dissipated per unit of pipe length is

$$\dot{W}' = \frac{\dot{m}}{\rho} \left(- \frac{dP}{dx} \right) = \pi \nu \tau_o Re, \quad (6)$$

where Re is the Reynolds number based on average velocity and pipe diameter. We obtain a second estimate for \dot{W}' by integrating the compact expression (5) over the pipe cross-section, introducing $y = r_o - r$ as the coordinate measured away from the pipe wall,

$$\dot{W}'_{\text{model}} = (2\pi \nu \tau_o) r_o^+ \int_0^{r_o^+} \left(1 - \frac{y^+}{r_o^+} \right) \left(\frac{du^+}{dy^+} \right) dy^+ \quad (7)$$

In writing equation (7) we took into account the fact that in turbulent pipe flow the apparent shear stress varies linearly with radial position [5],

$$(\nu + \epsilon_M) \frac{d\bar{u}}{dy} = \frac{\tau_o}{\rho} \left(1 - \frac{y}{r_o} \right). \quad (8)$$

The integral appearing on the right side of equation (7) can be evaluated by invoking one of the correlations for the universal velocity profile $u^+(y^+)$, for example, the von Karman three-segment correlation [5],

$$u^+ = y^+ \quad ; \quad 0 < y^+ < 5$$

AD-A123 321

ANALYTICAL PREDICTION OF TURBULENT HEAT TRANSFER
PARAMETERS(U) COLORADO UNIV AT BOULDER DEPT OF
MECHANICAL ENGINEERING A BEJAN DEC 82 CUMER-82-6

2/2

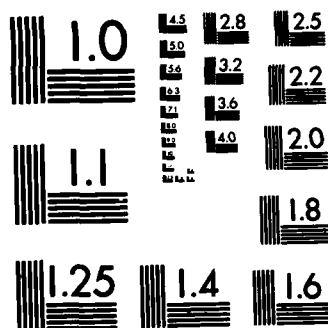
UNCLASSIFIED

N00014-79-C-0006

F/G 20/4

NL





MICROCOPY RESOLUTION TEST CHART
NATIONAL BUREAU OF STANDARDS-1963-A

$$u^+ = -3.05 + 5 \ln y^+ ; \quad 5 < y^+ < 30$$

$$u^+ = 5.5 + 2.5 \ln y^+ ; \quad 30 < y^+$$

Dividing equation (7) by equation (6) we obtain an integral measure of the deviation of model (5) from experimental findings,

$$\frac{\dot{w}'_{\text{model}}}{\dot{w}'} = \frac{5 \ln r_o^+ + 3.142 + 1958/r_o^+}{4.919 \ln r_o^+ + 3.983} \quad (9)$$

Visual inspection of this result leads to the conclusion that the test ratio $\dot{w}'_{\text{model}}/\dot{w}'$ is of order one, regardless of the value of the Reynolds number (r_o^+ or Re). This conclusion is emphasized by the following table of principal values:

Re	r_o^+	$\dot{w}'_{\text{model}}/\dot{w}'$
10^4	310.2	0.9973
10^5	2367.4	1.0014
10^6	19046.9	1.0043

The agreement between model (5) and experiment is exceptional: better than 0.5% in the range $10^4 < Re < 10^6$.

Conclusion

This note presented strong evidence that the expression

$$\epsilon = (\nu + \epsilon_M) \left(\frac{d\bar{u}}{dr} \right)^2 \quad (10)$$

accounts for the local dissipation rate in turbulent pipe flow. This compact expression is recommended by the symmetry between the momentum

equations for laminar flow and time-averaged turbulent flow. Based on what is known at this time, expression (10) can be regarded as "exact" in the viscous sublayer and "approximate" everywhere else in the turbulent core. However, in view of the success of the integral test (9), and in view of the fact that the viscous sublayer accounts for roughly half of the total dissipation rate \dot{W} [6], the error associated with using expression (10) in the turbulent core may be quite small.

The engineering importance of the present result stems from its compact form and from the fact that it is based on universal, readily available, turbulent flow measurements.

References

1. Bejan, A., "A Study of Entropy Generation in Fundamental Convective Heat Transfer", Journal of Heat Transfer, Vol. 101, 1979, p. 718.
2. Hinze, J.O., Turbulence, McGraw-Hill, New York, 1975, 2nd ed., p. 715.
3. Laufer, J., NACA Technical Report No. 1174, 1954.
4. Hildebrand, F.B., Advanced Calculus for Applications, Prentice-Hall, Englewood Cliffs, New Jersey, 1962, p. 355.
5. Rohsenow, W.M. and Choi, H.Y., Heat, Mass and Momentum Transfer, Prentice-Hall, Englewood Cliffs, New Jersey, 1961, pp. 72, 184.
6. Bejan, A., "Compact Expression for Viscous Dissipation in Turbulent Pipe Flow", Report CUMER 81-3, Department of Mechanical Engineering, University of Colorado, Boulder, 1981.

Nomenclature

D	pipe diameter
I	integral
\dot{m}	mass flowrate
P	pressure
r	radial position
r_o	pipe radius
r_o^+	Reynolds number based on radius and friction velocity, $r_o \sqrt{\tau_o / \rho} / \nu$
Re	Reynolds number based on diameter and average velocity
u	longitudinal velocity
u^+	dimensionless velocity $u / \sqrt{\tau_o / \rho}$
\dot{W}	pumping power dissipated per unit of pipe length
x	longitudinal position
y	distance away from the wall, $y = r_o - r$.
y^+	dimensionless wall distance, $y \sqrt{\tau_o / \rho} / \nu$
$(\bar{})$	time-averaged quantity
ϵ	local rate of viscous dissipation per unit mass
ϵ_M	eddy diffusivity for momentum
μ	viscosity
ν	kinematic viscosity
ρ	density
τ_o	wall shear stress

DISTRIBUTION LIST

HEAT TRANSFER

One copy except
as noted

Mr. M. Keith Ellingsworth
Materials and Mechanics Programs
Office of Naval Research
800 N. Quincy Street
Arlington, VA 22203

5

Defense Documentation Center
Building 5, Cameron Station
Alexandria, VA 22314

12

Technical Information Division
Naval Research Laboratory
4555 Overlook Avenue SW
Washington, DC 20375

6

Professor Paul Marto
Department of Mechanical Engineering
US Naval Post Graduate School
Monterey, CA 93940

Professor Bruce Rankin
Naval Systems Engineering
US Naval Academy
Annapolis, MD 21402

Office of Naval Research Eastern/
Central Regional Office
Bldg 114, Section D
666 Summer Street
Boston, Massachusetts 02210

Office of Naval Research Branch Office
536 South Clark Street
Chicago, Ill. 60605

Office of Naval Research
Western Regional Office
1030 East Green Street
Pasadena, CA 91106

Mr. Charles Miller, Code 05R13
Crystal Plaza #6
Naval Sea Systems Command
Washington DC 20362

Steam Generators Branch, Code 5222
National Center #4
Naval Sea Systems Command
Washington, DC 20362

Heat Exchanger Branch, Code 5223
National Center #3
Naval Sea Systems Command
Washington, DC 20362

Mr. Ed Ruggiero, NAVSEA 08
National Center #2
Washington, DC 20362

Dr. Earl Quandt Jr., Code 272
David Taylor Ship R&D Center
Annapolis, MD 21402

Mr. Wayne Adamson, Code 2722
David Taylor Ship R&D Center
Annapolis, MD 21402

Dr. Win Aung
Heat Transfer Program
National Science Foundation
Washington, DC 20550

Mr. Michael Perlsweig
Department of Energy
Mail Station E-178
Washington, DC 20545

Dr. W.H. Thielbahr
Chief, Energy Conservation Branch
Dept. of Energy, Idaho Operations Office
550 Second Street
Idaho Falls, Idaho 83401

Professor Ephriam M. Sparrow
Department of Mechanical Engineering
University of Minnesota
Minneapolis, Minnesota 55455

Professor J.A.C. Humphrey
Department of Mechanical Engineering
University of California, Berkeley
Berkeley, California 94720

Professor Brian Launder
Thermodynamics and Fluid Mechanics Division
University of Manchester
Institute of Science & Technology
PO88 Sackville Street
Manchester M601QD England

Professor Shi-Chune Yao
Department of Mechanical Engineering
Carnegie-Mellon University
Pittsburgh, PA 15213

Professor Charles B. Watkins
Chairman, Mechanical Engineering Department
Howard University
Washington, DC 20059

Professor Adrian Bejan
Department of Mechanical Engineering
University of Colorado
Boulder, Colorado 80309

Professor Donald M. McEligot
Department of Aerospace and Mechanical Engineering
Engineering Experiment Station
University of Arizona 85721

Professor Paul A. Libby
Department of Applied Mechanics and Engineering Sciences
University of California San Diego
Post Office Box 109
La Jolla, CA 92037

Professor C. Forbes Dewey Jr.
Fluid Mechanics Laboratory
Massachusetts Institute of Technology
Cambridge, Massachusetts 02139

Professor William G. Characklis
Dept. of Civil Engineering and Engineering Mechanics
Montana State University
Bozeman, Montana 59717

Professor Ralph Webb
Department of Mechanical Engineering
Pennsylvania State University
208 Mechanical Engineering Bldg.
University Park, PA 16802

Professor Warren Rohsenow
Mechanical Engineering Department
Massachusetts Institute of Technology
77 Massachusetts Avenue
Cambridge, Massachusetts 02139

Professor A. Louis London
Mechanical Engineering Department
Bldg. 500, Room 501B
Stanford University
Stanford, CA 94305

Professor James G. Knudsen
Associate Dean, School of Engineering
Oregon State University
219 Covell Hall
Corvallis, Oregon 97331

Professor Arthur E. Bergles
Mechanical Engineering Department
Iowa State University
Ames, Iowa 50011

Professor Kenneth J. Bell
School of Chemical Engineering
Oklahoma State University
Stillwater, Oklahoma 74074

Dr. James Lorenz
Component Technology Division
Argonne National Laboratory
9700 South Cass Avenue
Argonne, Illinois 60439

Dr. David M. Eissenberg
Oak Ridge National Laboratory
P.O. Box Y, Bldg. 9204-1, MS-0
Oak Ridge, Tennessee 37830

Dr. Jerry Taborek
Technical Director
Heat Transfer Research Institute
1000 South Fremont Avenue
Alhambra, CA 91802

Dr. Simion Kuo
Chief, Energy Systems
Energy Research Laboratory
United Technology Research Center
East Hartford, Connecticut 06108

Mr. Jack Yampolsky
General Atomic Company
P.O. Box 81608
San Diego, CA 92138

Mr. Ted Carnavos
Noranda Metal Industries, Inc.
Prospect Drive
Newtown, Connecticut 06470

Dr. Ramesh K. Shah
Harrison Radiator Division
General Motors Corporation
Lockport, New York 14094

Dr. Ravi K. Sakhuja
Manager, Advanced Programs
Thermo Electron Corporation
101 First Avenue
Waltham, Massachusetts 02154

Mr. Robert W. Perkins
Turbotec Products, Inc.
533 Downey Drive
New Britain, Connecticut 06051

Dr. Keith E. Starner
York Division, Borg-Warner Corp.
P.O. Box 1592
York, PA 17405

Mr. Peter Wishart
C-E Power Systems
Combustion Engineering, Inc.
Windsor, Connecticut 06095

Mr. Henry W. Braum
Manager, Condenser Engineering Department
Delaval
Front Street
Florence, New Jersey 08518

Dr. Thomas Rabas
Steam Turbine-Generator Technical Operations Division
Westinghouse Electric Corporation
Lester Branch
P.O. Box 9175 N2
Philadelphia, PA 19113

Dr. Al Wood
Director, Mechanics Program
Office of Naval Research
800 N. Quincy Street
Arlington, VA 22203

Mr. Walter Ritz
Code 033C
Naval Ships Systems Engineering Station
Philadelphia, Pa 19112

Mr. Richard F. Wyvill
Code 5232
NC #4
Naval Sea Systems Command
Washington, DC 20362

Mr. Doug Marron
Code 5231
NC #4
Naval Sea Systems Command
Washington, DC 20362

Mr. T. M. Herder
Bldg. 46462
General Electric Co.
1100 Western Avenue
Lynn, MA 01910

Mr. Ed Strain
AiResearch of Arizona
Dept. 76, Mail Stop 301-2
P. O. Box 5217
Phoenix, AZ 85010
(Tel. 602-267-2797)

Mr. Norm McIntire
Solar Turbines International
2200 Pacific Highway
San Diego, CA 92101

Prof. Daryl Metzger
Chairman, Mechanical and Energy
Systems Engineering
Arizona State University
Tempe, AZ 85281

END

FILMED

2-83

DTIC